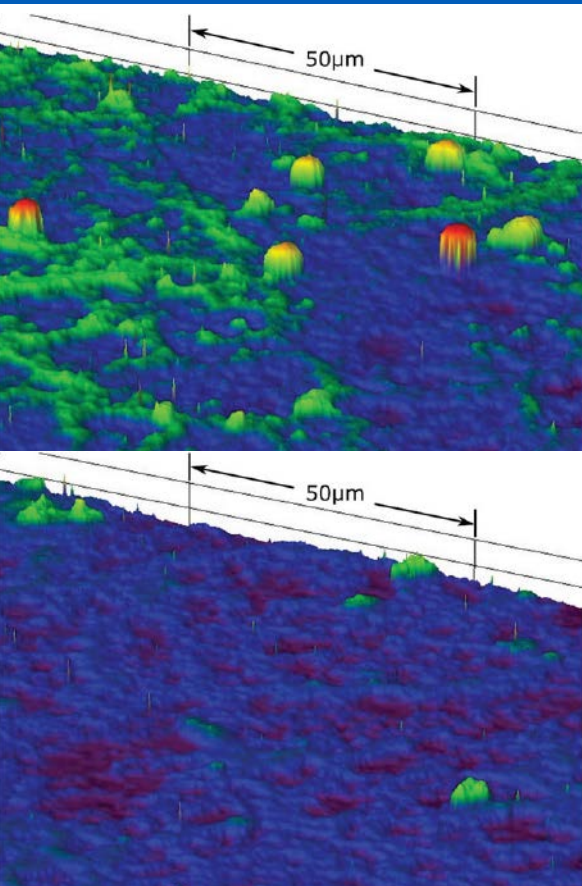


# 13

## Thin Films III

### Spray Coating Experiments: Setups and Methodologies



# Contents

- 3 Introduction  
Spray coating experiments: Setups and methodologies
- 6 A new paradigm for scalable fabrication of multilayer dielectric elastomer actuators  
**A. J. Cohen, M. Kolloche, M. C. Yuen, et al.**
- 15 Thick polymer films with self-healing, UV-protection, and anti-fog properties  
**N. H. Kashem, X. Liu, Z. Ding, et al.**
- 23 Enhancing the properties of electrodeposited copper foils by composite additives  
**S. P. Wang, K. X. Wei, W. Wei, et al.**
- 28 The art of science: Evident image of the year award 2022  
**Dr. Cecilia Kruszynski & Róisín Murtagh**

## Imprint

© Wiley-VCH GmbH  
Boschstr. 12,  
69469 Weinheim, Germany  
Email: [info@wiley-vch.de](mailto:info@wiley-vch.de)  
Editors:  
Dr. Cecilia Kruszynski &  
Róisín Murtagh

# Introduction

## Spray coating experiments: Setups and methodologies

Objects, tools, and structures that are designed for specific applications have specific requirements. In this context, the choice of materials is of crucial importance. However, it is difficult for a single material to meet all the requirements for a particular application. This is where coatings come into play. Coatings are used in the same way as other processes – such as heat treatments or alloying – to improve the properties of a material and adapt it to an application's requirements.

Coatings provide various properties, such as corrosion/wear resistance, hardness enhancement, tailored textures, thermal and electrical insulation, and tailored wettability.<sup>[1]</sup> In addition, coating processes provide tools for the fabrication of layered nanocomposites, which play a key role in fundamental science and technology.<sup>[2,3]</sup>

There is an extensive variety of coating methods. However, due to their effectiveness and applicability, the most employed ones include physical vapor deposition, chemical vapor deposition, sol-gel, and spray coating.<sup>[4]</sup>

Spray coating is a technique based on the impingement of particles onto a surface, and it constitutes a widespread method for rapid, large-scale homogeneous coating. Spray deposition is relevant for a broad range of applications, like energy-saving and storage applications, photovoltaic, foils, semiconductors, and catalysis, among others.<sup>[5]</sup> Moreover, spray coating enables simple layer-by-layer (LbL) approaches and easy deposition of functional layers on flexible substrates and devices, especially electrodes.<sup>[6]</sup>

Spray coating can be roughly classified into two groups: thermal spray and cold spray. The

main difference between them is that the cold spray technique does not require a combustion process like most thermal spray applications. Cold spray relies on kinetic energy using high speeds to deform the material particles and adhere them to the surface of the object. Cold spray and thermal spray differ in the coating materials and the resulting coating properties.

Thermal spray coatings use a heat source – plasma, electrical, or chemical combustion – to melt a series of specific materials and spray the melt onto the surface at a high jet speed. The coating thicknesses achieved range from 20  $\mu\text{m}$  to several millimeters, which is significantly higher than the thickness offered by electroplating, chemical vapor deposition, or physical vapor deposition processes.<sup>[7]</sup> The feedstock for thermal spray coatings ranges from refractory metals and metal alloys to ceramics, plastics, and composites, and can easily cover a relatively large surface area of a substrate.<sup>[7]</sup> The most common types of thermal coating processes are plasma, detonation, hot/cold, high-velocity air fuel (HVOF), high-velocity oxygen (HVOF), flame, and arc spraying.<sup>[4]</sup>

There are two main types of cold-air spraying: low-pressure and high-pressure performance. Some cold-air spray systems use com-

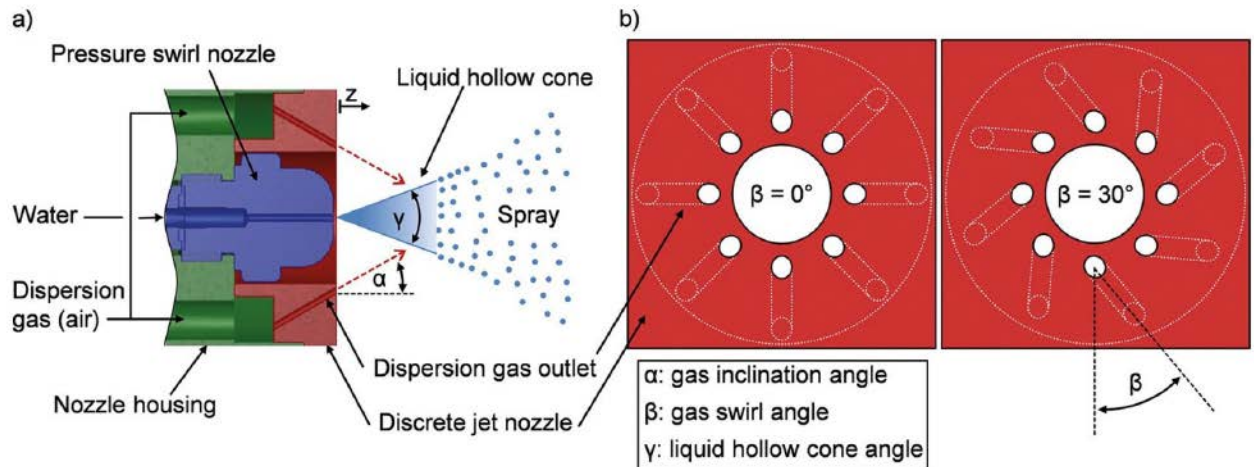


**Figure 1:** a) Liquid hollow cone nozzle (pressure swirl nozzle) adapted with dispersion gas nozzle (discrete jet nozzle); cross-sectional view at the nozzle center plane, illustrating the gas inclination angle,  $\alpha$ . b) Top view of two discrete jet nozzles, illustrating the influence of the gas swirl angle,  $\beta$  on the orientation of dispersion gas outlets.<sup>[8]</sup>

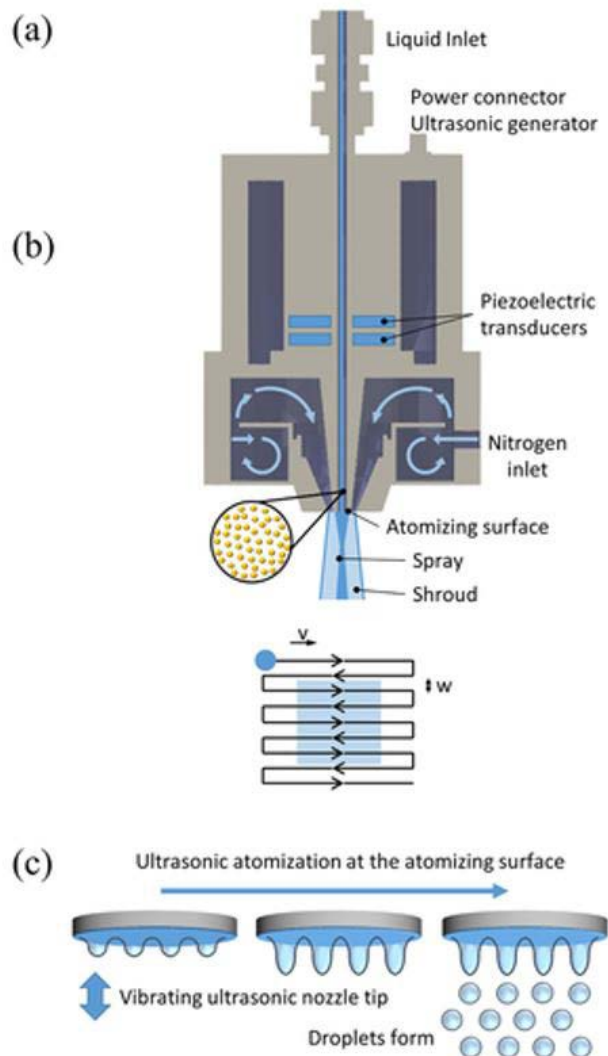
pressed air to turn the coating liquid into a fine mist that is sprayed onto the target. The compressed air exerts high pressure on the coating fluid exiting the nozzle, which then impacts the remaining air at high velocity. At this moment, the coating liquid is split and slowed down due to the air resistance and then turns into a mist before reaching the target, as schematically shown in **Figure 1a**.<sup>[8]</sup> Different products are available depending on the target area, required efficiency, and coating purpose.

Other systems, such as ultrasonic spray systems, are equipped with an atomization surface chip at the end of the nozzle. The vibration generated by the ultrasonic waves causes the coating liquid to spread on the chip, and surface rippling occurs. When the ultrasonic power exceeds the surface tension, the liquid drips from the surface as a fine mist (**Figure 2c**).<sup>[9]</sup> Because these systems can produce fine and uniform droplets, they are suitable for uniform coating of a limited area. Another advantage is that material loss is very low because the system causes almost no splashing or unnecessary dispersion of the coating liquid. The nozzle can be selected from many different lengths, sizes, and shapes depending on the purpose. The thickness and quality of the coating film can be controlled by adjusting the required flow rate and vibration frequency to ensure a uniform coating fluid spray. Applications of these systems include insulating and conductive coatings

on electronic components, semiconductor photoresists, hard coatings, anti-glare, and hydrophobic and oleophobic coatings.

Finally, in electrospray systems, the coating liquid is charged with static electricity by applying several thousand volts in the nozzle. The liquid is then transformed into a fine mist by electrostatic repulsion. The mist of the coating liquid is attracted to the surface of the target, which is located on a grounded stage. These systems can be used for liquids with different viscosities as well as pastes, slurries, and liquids with filler dispersions. The result is a uniform film, even on substrates with uneven surfaces. Since almost all the coating liquid can be applied only to the surface of the substrate, the efficiency of liquid consumption is significantly higher than with typical air spray coaters and spin coaters. As a result, material costs can be reduced.

Spray coating technology, with its many variations, is a versatile tool for producing single layers in the nanometer to millimeter range. This versatility is of key interest in the field of coatings and films. In addition, spray coating processes offer several advantages, such as high speed, large manufacturing area, and low cost, which make them attractive for the production of the multilayer composites used in various technology areas.



## REFERENCES

- [1] B. Bhushan and B. K. Gupta, "Handbook of tribology: materials, coatings, and surface treatments," 1991.
- [2] J. Prakash, J. C. Pivin, and H. C. Swart, "Noble metal nanoparticles embedding into polymeric materials: From fundamentals to applications," *Adv. Colloid Interface Sci.*, vol. 226, pp. 187–202, Dec. 2015, doi: 10.1016/j.cis.2015.10.010.
- [3] F. Faupel, V. Zaporozhchenko, T. Strunskus, and M. Elbahri, "Metal-Polymer Nanocomposites for Functional Applications," *Adv. Eng. Mater.*, vol. 12, no. 12, pp. 1177–1190, Dec. 2010, doi: 10.1002/adem.201000231.
- [4] B. Fotowati, N. Namdari, and A. Dehghanghadikolaei, "On Coating Techniques for Surface Protection: A Review," *J. Manuf. Mater. Process.*, vol. 3, no. 1, p. 28, Mar. 2019, doi: 10.3390/jmmp3010028.
- [5] S. V Roth, "A deep look into the spray coating process in real-time – the crucial role of x-rays," *J. Phys. Condens. Matter*, vol. 28, no. 40, p. 403003, Oct. 2016, doi: 10.1088/0953-8984/28/40/403003.
- [6] S. Sorel, U. Khan, and J. N. Coleman, "Flexible, transparent dielectric capacitors with nanostructured electrodes," *Appl. Phys. Lett.*, vol. 101, no. 10, p. 103106, Sep. 2012, doi: 10.1063/1.4750059.
- [7] L. Pawlowski, *The Science and Engineering of Thermal Spray Coatings*. Wiley, 2008.
- [8] F. Meierhofer, M. Hodapp, L. Achelis, L. Buss, D. Noriler, H. F. Meier, and U. Fritsching, "Investigation of atomization concepts for large-scale flame spray pyrolysis (FSP)," *Mat.-wiss. u. Werkstofftech.*, vol. 45, p. 765–778, 2014, doi: <https://doi.org/10.1002/mawe.201400314>.
- [9] J. Stryckers, T. Swusten, W. Brullot, J. D'Haen, T. Verbiest, and W. Deferme, "Ultrasonic Spray Coating as a Fast Alternative Technique for the Deposition of Hybrid Magnetic-Plasmonic Nanocomposites," *Adv. Eng. Mater.*, vol. 20, p. 1800681, 2018, doi: <https://doi.org/10.1002/adem.201800681>.

**Figure 2:** a) Cross-section of the used ultrasonic spray nozzle. b) Track followed during deposition. c) Ultrasonic atomization principle at the atomizing surface.<sup>[9]</sup>

# 01 A new paradigm for scalable fabrication of multilayer dielectric elastomer actuators

A. J. Cohen, M. Kolloche, M. C. Yuen, *et al.*

Multilayer dielectric elastomer actuators have a wide range of potential applications, but their development and commercial implementation have been hindered by existing manufacturing processes. Existing processes are low throughput, limited in area, and/or can only process a narrow range of elastomers. This study presents a novel fabrication paradigm that overcomes these challenges: instead of sequentially patterning electrodes directly onto successive elastomer layers, electrode stamps are patterned onto a carrier film in an independent batch-spray process, and the electrodes are then stamp-transferred onto each elastomer layer. The capabilities of this process to produce useful devices are demonstrated with a large-area loud-speaker and an actuator with 60 active layers.

## INTRODUCTION

More than 20 years after Pelrine *et al.*<sup>[1]</sup> catalyzed research into soft, energy-dense dielectric elastomer actuators (DEAs), DEAs are still not commercially relevant. Many challenges have already been addressed; however, the manufacturing of multilayer DEAs (MDEAs) remains a barrier to their widespread adoption.

MDEAs are crucial for generating large forces and displacements without excessively high voltages. Comprised of tens to hundreds of thin (typically 10–100  $\mu\text{m}$ ) DEA layers that have been stacked atop each other, MDEAs' force and displacement outputs scale proportionally with the number of layers, and they can be arbitrarily scaled to meet the applica-

tion-specific force and displacement requirements without requiring changes to actuator design, materials, or drive electronics.

Fabricating MDEAs remains a key technical challenge for their widespread use. First, many electrode layers must be alternated with an equal number of thin, delicate elastomer layers. Second, these electrodes must meet several performance requirements: they must be conductive ( $<100 \text{ k}\Omega\text{sq.}^{-1}$ ), stretchable ( $>100\%$  elongation), and contribute minimal stiffness to the MDEA composite structure ( $<10\%$ ). Finally, they must not reduce the breakdown strength of the elastomer.

For scalability to an industrial process, it must also be possible to produce large-area elec-

trodes and quickly deposit them onto the elastomer surface. To be useful in a variety of applications, the electrodes must also be compatible with a wide range of elastomers.

We propose the following criteria should be met by a laboratory-scale MDEA fabrication process:

- 1) high throughput (10 layers  $h^{-1}$ ).
- 2) large electrode area (at least  $250 \times 250$  mm).
- 3) a wide range of compatible elastomer materials.

Electrode deposition processes in which a wet electrode ink contacts an elastomer layer tend to introduce complications due to the many solvent-elastomer interactions, which might cause dimensional changes and long-term degradation under an electric field. This either leads to a limited set of usable elastomers or significant tuning, which could slow the process's adoption for new applications. Scaling to industrial levels also requires that each subprocess does not impose fundamental physical or practical limitations on the key criteria of throughput, electrode area, or compatible elastomers.

Our multilayer DEA fabrication method, illustrated in **Figure 1**, overcomes these challenges by splitting electrode deposition into two independent processes: electrode spraying and electrode stamping. First, carbon black (CB) electrodes are sprayed onto a masked substrate in large batches. The electrodes, made of a network of loose powder, can then be quickly and easily stamp-transferred onto successive elastomer layers to construct the MDEA. This dramatically reduces the sequential portion of electrode deposition that limits throughput, allowing us to achieve 15 layers  $h^{-1}$  at laboratory scales. The batch spraying is also easy to scale to larger electrode areas by modifying the size of the spray gantry's raster path and using larger substrates. Unlike wet-deposition methods, dry stamping also has no solvent-elastomer interactions, which would otherwise limit compatible elastomers or need intensive tuning of the process for each elastomer. This allows for the process to be used with a wide range of elastomers with minimal tuning. The modularity of the batch-spray and stamp-transfer paradigm provides a flexible platform that may be customized to meet application-specific requirements.

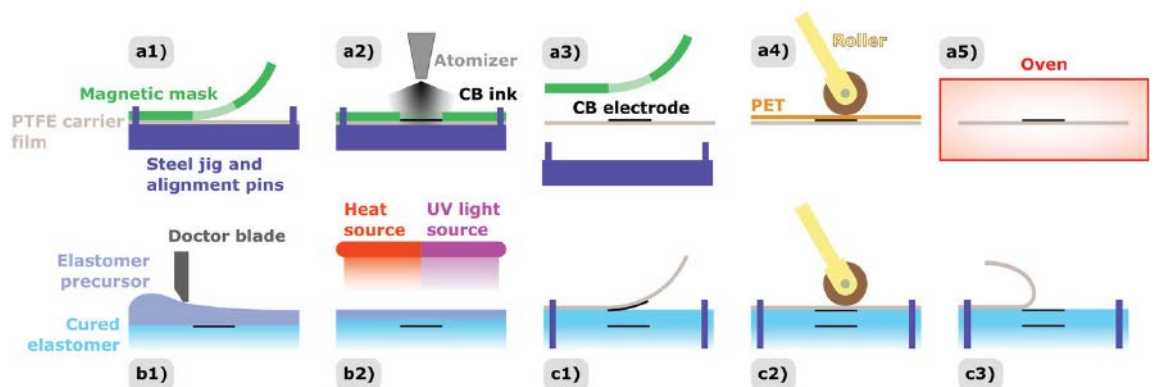


**Figure 1:** Diagram of the batch-spray and stamp-transfer process. a) CB electrodes are batch-sprayed. a1) A magnetic mask with a stencil of the desired pattern is aligned with pins and placed atop the PTFE carrier film. a2) CB ink is atomized and sprayed onto the masked carrier film. a3) The magnetic mask is removed, and the carrier film with patterned electrodes on it is removed from the jig. a4) A sheet of polyethylene terephthalate (PET) is placed on top of the electrodes, and a roller is used to apply pressure and reduce peaks on the electrode surface. a5) The roll-treated electrodes are stored in an oven at 70 °C (158 °F) to keep them dry until they are used. b) An elastomer layer is deposited. b1) Elastomer precursor is deposited on top of the last electrode layer and is then b2) cured with UV light or a heat source depending on the elastomer cure requirements. While this diagram uses doctor blading as a representative elastomer deposition process, other deposition processes could be used. c) An electrode is stamped onto the elastomer surface. c1) A face-down electrode is aligned with the multilayer using alignment pins; c2) a roller applies pressure to the back of the carrier film, ensuring consistent contact and transfer of the CB powder to the elastomer; and c3) the carrier film is lifted away, leaving the electrode patterned on the surface. Steps (b) and (c) are repeated until the desired number of layers has been reached.

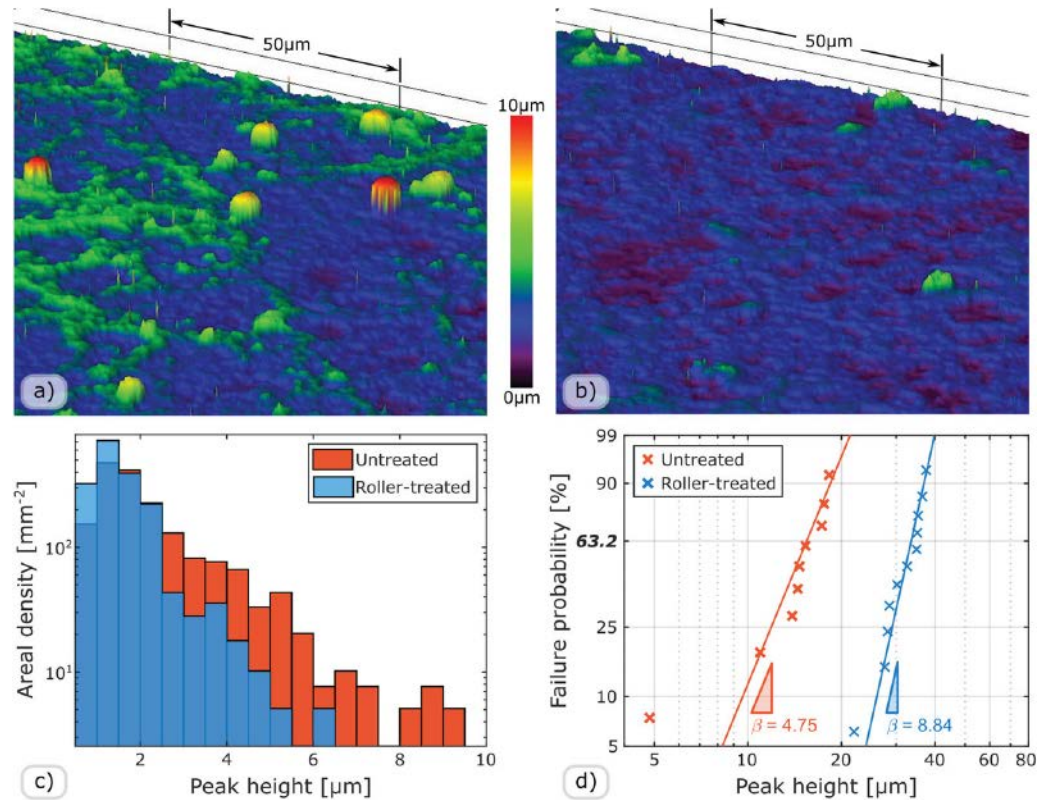


**Figure 2:** Effect of mechanical treatment on electrode topology and DEA breakdown strength. a) An Olympus OLS4000 laser microscope was used to obtain a height map of the surface of an untreated electrode while it was still on the PTFE carrier film. Many high peaks of about 10 μm are visible. b) After mechanical treatment, these peaks are dramatically reduced. As shown by this representative height map of an electrode after treatment, peaks higher than 5 μm are mostly eliminated. c) Six 256 × 256 μm images were taken at random points across electrodes from the same batch, before and after mechanical treatment. Peak-finding code was used to identify all peaks in the 2D image space, and the distribution of their heights is plotted as a histogram. Peaks shorter than 0.5 μm are not shown. The higher peaks have been dramatically reduced in number because of the treatment. This likely reduces localized surface stresses and field concentrations that would cause a premature electrical breakdown. d) The Weibull plot shows 11 treated and nine untreated specimens tested to failure. Each data point represents the breakdown field of a single specimen, fit to a Weibull distribution. The plot indicates that the treated specimens show over 100% higher breakdown strength  $E_b$ , compared to the untreated – 33.5 versus 15.7 V μm<sup>-1</sup>. The treated electrodes are also more consistent, with a Weibull shape factor of  $\beta_{\text{treated}} = 8.84$  versus  $\beta_{\text{untreated}} = 4.75$ .

## RESULTS

### Fabrication Process

For this study, we used CB dispersed in isopropanol (IPA) as a sprayable electrode dispersion. Both CB and IPA are inexpensive and widely available, making the ink cheap and easy to produce. The ink was dispensed with a peristaltic pump, broken into micron-sized droplets with an ultrasonic atomizer (Son-aer, NS130K), and ejected onto a polytet-

rafluoroethylene (PTFE) carrier substrate that has been masked with a vinyl-cut magnetic stencil of the desired electrode pattern. This powder stamp can transfer even to minimally tacky elastomers. Moreover, it avoids an extra binder-curing step and does not contain any solvent that could swell or bead up on the elastomer layer it contacts.

After the electrodes are sprayed, we mechanically treated them to roughly double the break-

down strength. A roller is used to apply pressure to a layer of PET atop the sprayed electrode, and this step is repeated a second time. **Figure 2** shows how this produces a much flatter topology, reducing the prevalence of peaks higher than  $5\ \mu\text{m}$  from  $120$  to  $13\ \text{mm}^2$ . This reduction in peaks can lower the electrical field concentrations, which could result in premature dielectric failure (breakdown).

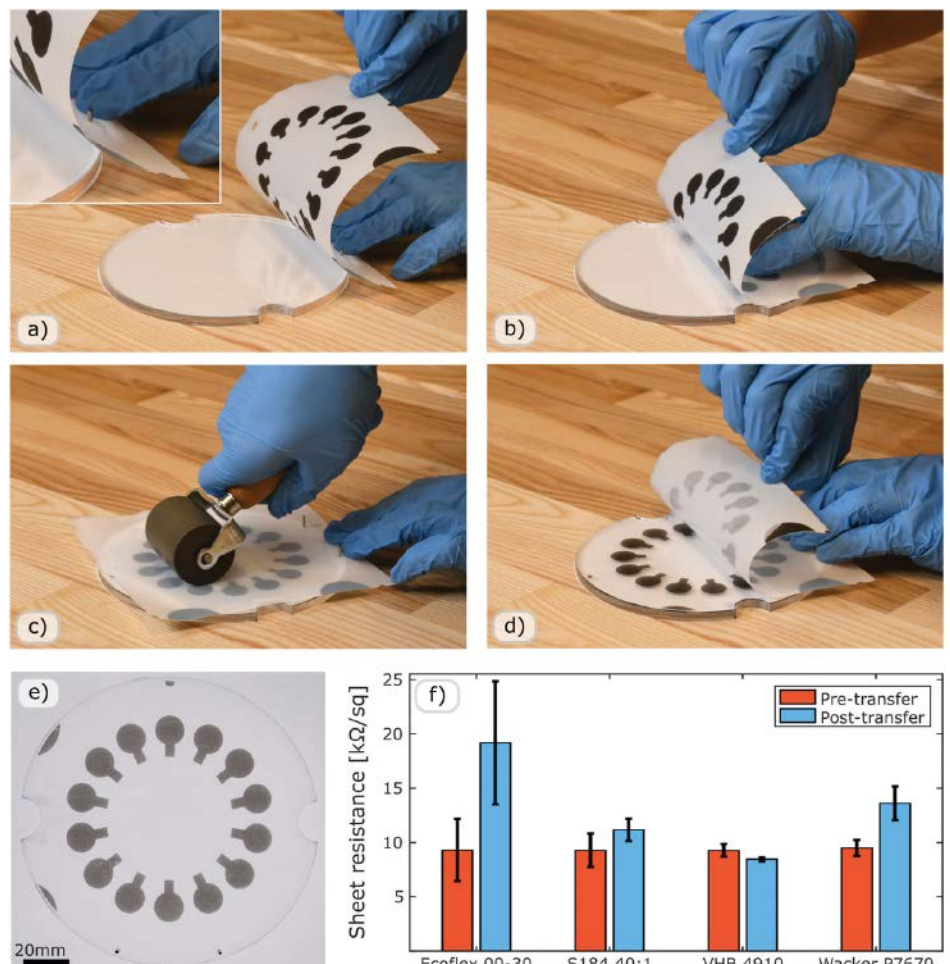
The electrodes are assembled into MDEAs by using pins and precut alignment holes in the substrates to align them with a cured elastomer substrate. In this study, we used Elastosil P7670 A/B (Wacker Chemie AG). To ensure that the CB transfers to the elastomer, a roller is used to apply pressure to the back of the carrier film. **Figure 3** demonstrates how the CB transfers to the elastomer as the carrier film is peeled off the elastomer. The final thickness of the transferred electrode on the P7670 is approximately  $240\ \text{nm}$ . The entire alignment

and stamping process requires approximately 1–2 min by hand and could be accelerated with an automated roll-to-roll setup. Because the carrier film is flexible, it is also possible to transfer electrodes onto curved surfaces.

An elastomer layer is then deposited, degassed, and cured on the existing stack, and an electrode is stamp-transferred. This procedure is repeated until the desired number of layers has been reached. Excluding the elastomer-dependent cure and degas times, this process takes only 4 min per layer (2 min each for the deposition and transfer steps).

Each of the batch-spray and stamp fabrication steps could also be implemented as a roll-to-roll process to dramatically increase throughput and electrode area for industrial-scale production. The carrier film and mask are already sheets, and thus could be easily processed as a web. The web would also

**Figure 3:** The electrode stamp-transfer process is demonstrated with a set of breakdown test electrodes on a  $30\ \mu\text{m}$  P7670 film spin-coated onto an acrylic substrate and cured. After the previously described mechanical treatment, the full  $300\times 300\ \text{mm}$  sheet was cut with scissors into fourths for transfer onto a smaller,  $150\ \text{mm}$  diameter substrate. a) Precut alignment holes in the PTFE carrier film are aligned with pins in corresponding alignment holes in the acrylic substrate. b) The carrier film is rolled out onto the elastomer substrate. c) A roller is used to stamp-transfer the electrodes onto the elastomer. d) The PTFE film is removed and either discarded or cleaned and reused. After this step, an anti-static gun is used on the surface to prevent dust accumulation. e) An overhead view of the final transferred electrode. f) Effect of transferring the electrode from carrier film to various elastomer substrates. Each bar represents the mean sheet resistance of  $20\ \text{mm}$  specimens ( $n = 3$ ) measured both before and after the transfer operation using a 4-point probe. Error bars represent  $\pm$  one standard deviation.



serve to align each element. Similarly, elastomers could be deposited on a web using doctor blading and the electrode could be stamped and treated using rolling presses. The ink deposition can be accelerated by simply setting a higher flow rate on the pump, making the ink in larger batches, and moving the web underneath a row of nozzles.

## ELECTRODE CHARACTERIZATION

The resistance-strain behavior of the electrodes was examined using a dog bone-shaped electrode design stacked into multilayers of five 30  $\mu\text{m}$  elastomer layers and four 10 $\times$ 25 mm electrode layers. A comparison of a set of samples with and without CB electrodes indicates no impact of the electrodes on the stiffness at either small or large strains. The electrodes also remained conductive until they mechanically ruptured (at 225% strain). Furthermore, they exhibited suitable linearity below 100% strain with a gauge factor (GF) of  $5.4 \pm 0.13$  for the chosen design. The measured resistance during cyclic experiments exhibits hysteresis, but this hysteresis decreases and then stabilizes; the ratio of the area inside the hysteresis loop  $\Delta A$  to the total area under the first loading curve  $A_0$  decreases from 14.8% on the first cycle to 6.7% on the 100<sup>th</sup>. These electromechanical characteristics may also make the electrode suitable for use as soft strain sensors or as energy harvesters.

Breakdown tests were performed on encapsulated single-layer DEAs produced with batch-sprayed electrodes. A 10  $\text{V s}^{-1}$  voltage ramp was applied across the 32.7  $\mu\text{m}$  P7670 DEA layer until the device experienced electrical failure (breakdown). As indicated in **Figure 2d**, our DEAs had a breakdown strength of 33.5  $\text{V } \mu\text{m}^{-1}$  and a shape factor of 8.84. This is comparable to actuators made by Chortos<sup>[2]</sup> and Kiil<sup>[3]</sup>, which achieved strengths of 25 and 40  $\text{V } \mu\text{m}^{-1}$ , respectively. The upper bound of breakdown strength for a DEA, however, should be that of the pure elastomer. Using<sup>[4]</sup>, we found the breakdown strength of the P7670 to be 64  $\text{V } \mu\text{m}^{-1}$  with a shape factor of 9.33.

Some of the difference between breakdown strength with and without CB electrodes is likely due to the contact area of the electrodes being approximately 20 times larger than that of the pure material test setup, increasing the chance of defects in the enclosed elastomer. The remaining defects in the electrodes likely

also reduce the breakdown strength, reducing their relative influence by increasing the elastomer thickness to 71.4  $\mu\text{m}$  yielding an enhanced breakdown strength of 41.2  $\text{V } \mu\text{m}^{-1}$ . These breakdown characteristics may thus be further improved in the future by tuning the mechanical treatment process or reducing the presence of agglomerations in the ink. This would enable even larger and more energy-dense actuators.

## DEMONSTRATION OF DEVICES

A DEA subwoofer was selected to illustrate the functionalities enabled by the large electrodes that can be produced with this process. The speaker is comprised of a 200 mm diameter single-layer DEA stretched over an air-pressurized chamber. The DEA was created by first doctor-blading, degassing, and fully curing a 70  $\mu\text{m}$  film of P7670. Doctor blading is readily scalable to large areas and is thus suitable for such large-area actuators. Electrodes patterned into the shape of a quartered disk were then stamped onto either side of the film. Each quarter had connection tabs to allow for independent testing of each segment.

The speaker's four quadrants were connected to a single Trek 2220 high-voltage amplifier, and the speaker was inflated to an approximately hemispherical shape with less than 10 kPa of pressure to enhance sound production. An audio file converted to a voltage signal was then supplied to the speaker via the amplifier, and the resulting audio was measured on a Shure SM57 microphone placed 25 cm away from the apex of the speaker membrane. As shown in **Figures 4b** and **c**, the speaker successfully replicated the input signal at the low frequencies required of a subwoofer. The maximum volume produced by the speaker was 45.6 dB SPL, as measured by Decibelxon an iPhone 13 Pro positioned at the same distance from the speaker, just below the primary SM57 microphone. Some noise can be heard from the sub-optimal recording environment. The buzzing in the audio can also be attributed to the method of clipping the audio signal when the supplied voltage would have exceeded the maximum voltage output of the amplifier.

An MDEA with 60 active layers was also fabricated to showcase the ability of the process to produce actuators with many layers. The MDEA is comprised of 12 stacks of seven elastomer and six electrode layers each (the outer two elastomer layers are inactive, and only

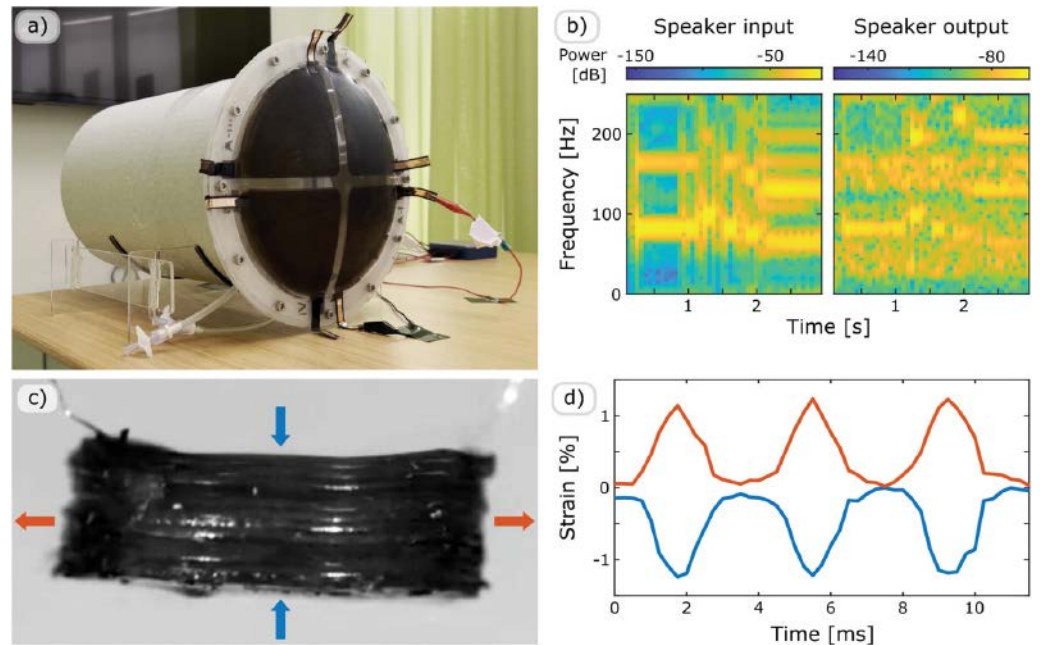


**Figure 4:** a) A view of the speaker from the front. The diameter of the membrane is 200 mm. b) A comparison of the speaker input and output spectrograms. Power measures are arbitrarily defined relative to the strength of the overall signal, not relative to sound pressure levels. The speaker is able to reproduce the low-frequency sounds (20–200 Hz) expected of a subwoofer. The decreased signal to noise ratio of the output is due to a combination of sub-optimal recording environment, relative weakness of the speaker compared to the original audio output, and clipping causing harmonic distortion at higher volumes. c) Side view of the 60-layer MDEA, with principal directions of strain indicated in orange and blue. The MDEA is suspended by its lead wires in a free displacement condition. d) Three selected strain cycles of the actuator in response to a 200 Hz, 0–2 kV sinusoidal input signal are plotted. The device reaches horizontal strains of 1.24% and vertical strains of 1.23%. Design improvements could likely yield increased strains in the future. Because only five out of seven elastomer layers were active and the electrodes were surrounded by a 1.25 mm margin, only 52% of the actuator's total volume was active.

serve to encapsulate the electrodes). Each of the elastomer layers was doctor-bladed to a thickness of 70  $\mu\text{m}$  and stamped with 15 mm diameter disk-shaped electrodes. These stacks were punched manually with a 17.5 mm hammer-driven hole punch and then manually laid atop each other to create the 6.0 mm-tall, 17.5 mm-diameter cylindrical MDEA seen in **Figure 6d**. Colloidal graphite paint was used to connect the exposed tabs of the electrodes to thin wires. The wire leads were then encapsulated in a small droplet of P7670 to prevent them from detaching.

The device was suspended by its connecting wires in a free displacement condition, and its wires were connected to a Trek 2220 amplifier. The amplifier actuated the device with a 200 Hz sinusoidal voltage signal rang-

ing from 0–2 kV. This caused the actuator to reach horizontal strains of 1.24% and vertical strains of 1.23%. Strains were calculated by taking high-speed video with a Phantom V2512 and using edge detection to find the perimeter of the device in each frame.

## CONCLUSION

We presented a high-throughput, large-electrode MDEA fabrication process that works with a wide range of elastomer materials. This combination of qualities provides a path to industrial-scale production of MDEAs. The electrodes produced via this process have been shown to be stretchable beyond 200%, add negligible stiffness to the soft structure, maintain their strain-resistance behav-

ior over at least 100 cycles, and have breakdown strengths of  $33.5 \text{ V } \mu\text{m}^{-1}$ . A large-area DEA subwoofer and 60-layer MDEA demonstrate the capabilities achievable with this batch-spray and stamp process.

## EXPERIMENTAL SECTION

*Ink preparation:* The electrode ink was prepared by dispersing Printex CB in IPA at a ratio of 0.125 wt% ( $0.95 \text{ mg mL}^{-1}$ ). The mixture was then sonicated in a glass bottle with a 12.5 mm diameter extended tip at an amplitude of 75% for 10 min, yielding an energy density of  $420 \text{ J mg}^{-1}$  of CB. To avoid significant sedimentation of the CB within the solution, a clean magnetic stir bar was placed into the bottle, and the bottle was placed on a magnetic stir plate.

*Substrate and mask preparation:* A PTFE carrier film was prepared by laser-cutting alignment holes. These holes allow for precise alignment of the carrier film and pattern mask during spraying and the electrode and multi-layer substrate during electrode stamping. It was then cleaned with distilled water, IPA, acetone, IPA again, and distilled water again and blown dry to remove any residual contamination. The mask material was a flexible, 750  $\mu\text{m}$  thick sheet of magnetized iron filings in a vinyl binder matrix. It can be reused for multiple batches of electrodes. The PTFE carrier film was placed onto a steel jig and the magnetic mask was placed atop it. The mask's magnetic attraction to the jig formed a tight seal around the edges of the pattern, ensuring sharp features. This jig assembly was then placed onto a hot plate set to  $80 \text{ }^\circ\text{C}$  ( $176 \text{ }^\circ\text{F}$ ).

*Batch spraying procedure:* A tube was inserted through the jar's lid, and a peristaltic pump dispensed the ink through this tube at a rate of  $0.8 \text{ mL min}^{-1}$ . An accumulator was connected at a junction in the line to prevent backflow and smooth flow variations. The ink then flowed into an atomizing nozzle which broke the stream into micron-scale droplets. These droplets were expelled from the nozzle using a 60 kPa air supply onto the surface of the carrier film, which was mounted 10 cm below the nozzle. The nozzle was mounted on a custom-built gantry, which swept the nozzle back and forth in a raster pattern over the surface of the carrier film. The sweep was repeated eight times at a feed rate of  $2,000 \text{ mm min}^{-1}$ , with 1 cm spacing between raster lines. The full path over a  $300 \times 300 \text{ mm}$  sheet required approximately 30 min to complete. Once the

deposition was complete, the carrier film was removed from the heat plate and covered.

*Mechanical treatment:* Once the PTFE carrier film had cooled to room temperature, the CB electrode on the carrier film was treated by manually pressing a sheet of 125  $\mu\text{m}$  polyethylene terephthalate (PET) onto it with a rubber roller with approximately 100 N of force. An anti-static gun was used to remove static from the sample's surface, which would otherwise attract dust particles. Once the electrode had been treated, it was covered and stored in an oven set to  $70 \text{ }^\circ\text{C}$  ( $158 \text{ }^\circ\text{F}$ ) to keep it dry.

*Stamp transfer testing:* To characterize the transfer of CB electrodes from the PTFE carrier to the elastomers, a batch of 25 electrode disks with diameters of 20 mm was sprayed and treated using the procedure described above. Sheet resistance was measured while the electrodes were still on the PTFE carrier using a 4-point probe connected to a Keithley 6221 current supply and Keithley 2182A nanovoltmeter. To avoid edge effects that could affect the measurement of sheet resistance, the 20 mm diameter of the electrodes used for testing sheet resistance was larger than that of the breakdown samples. LabView software was written to supply current and measure the resulting change in voltage. This was performed at three voltage steps and a line of best fit was taken to determine the resistance.

Films of various elastomers were produced by spin-coating onto glass or acrylic substrates. They were then allowed to completely cure. In the case of VHB 4910, a 1 mm thick tape was adhered to thick 250  $\mu\text{m}$  PET, with no extra curing required. Each of these elastomers was treated with an anti-static gun and placed in a large petri dish to prevent dust from accumulating on the exposed surface. For each elastomer, three disk electrodes were chosen as transfer samples. These electrodes were transferred to the elastomer surface using a soft roller to apply pressure. Immediately after the transfer, the sheet resistance was measured with the 4-point probe.

*Breakdown testing:* Breakdown tests were performed on single-layer DEAs 15 mm in diameter. The elastomer layer was produced by spin coating the uncured P7670 precursor onto a circular acrylic substrate at 1,500 RPM for 60 s. This yields a layer thickness of  $32.7 \pm 0.7 \text{ } \mu\text{m}$ . The precursor was then degassed in a vacuum chamber at room temperature for approximately 4 min and cured in an oven at

70 °C (158 °F) for approximately 4 min under a normal atmosphere. Once removed from the oven, batch-sprayed 15 mm diameter CB electrode disks were stamp-transferred onto the P7670. This was repeated once to form the DEA structure and then a final spin-coating step was used to encapsulate the parallel electrodes. The encapsulation best reproduced the conditions of an MDEA structure.

The design was electrically connected by cutting through the thickness of the devices and applying colloidal graphite paint to the exposed cross-sections. The paint was then extended to copper tape contacts, which were attached to the leads of a Trek 610 E high-voltage amplifier.

Breakdown tests were performed by applying a linear voltage ramp of  $10 \text{ V s}^{-1}$  up to 2 kV with the current limit set to  $30 \text{ }\mu\text{A}$ . The current was monitored, and the test was terminated once the operator noticed a sustained surge in current. The breakdown voltage was specifically defined as the highest voltage at which the current through the capacitor was below  $1 \text{ }\mu\text{A}$  for at least 0.25 s. This accounted for transient current spikes which occur before a catastrophic breakdown of the device. The voltage was divided by the elastomer thickness to yield the breakdown field.

*Electrode tensile testing:* Samples were prepared using patterning dog bone-shaped electrodes whose central beams were  $25 \times 10 \text{ mm}$ . Four of these were stamped onto successive doctor-bladed elastomer layers, each  $30 \text{ }\mu\text{m}$  thick. These samples were then cut out with a stencil to yield a rectangular sample of  $40 \times 25 \text{ mm}$ . Sections of the elastomer without any CB on it were similarly cut out to yield the elastomer-only samples, which were controlled for any change in stiffness due to the successive deposition and curing processes. The rectangular CB composites were then sliced such that the ends of the embedded electrodes were exposed. As with the breakdown samples, Pelco colloidal graphite paint was used to connect the electrodes to copper leads, to which the LCR meter's leads were attached.

For the resistance-strain characterization, an Instron tensile testing machine (5544A) equipped with a 10 N load cell was used to apply strains. All experiments were performed with a strain rate of  $1\% \text{ s}^{-1}$ . The electrode resistance was continuously measured with an LCR meter (Keysight E4980A) used in the CsRs mode at a frequency of 100 Hz with a 2 V medium average. To allow a synchro-

nous recording of force, strain, and resistance, a LabVIEW program was designed to connect the LCR meter with the control software of the Instron tensile tester (Bluehill V4.29). The rupture experiments were performed after first applying the 100 cycles of loading.

*MDEA demonstration device fabrication and assembly:* The 60-layer MDEA demonstration device was created by fabricating 12 shorter MDEA stacks and then assembling them into a single taller meta-stack. Each of the stacks was created in a single batch. The electrodes were of the same design as those used in breakdown experiments: 15 mm diameter disks with connection tabs. A mask with 72 of these electrodes on it was designed such that electrodes were grouped into six sets of 12 electrodes each, with each set having its own alignment holes. The electrodes were then spray-patterned as described in Section 2.1. A doctor blade was used to deposit a  $70 \text{ }\mu\text{m}$  Elastosil P7670 precursor layer on top of the existing stack. After degassing and curing the layer for 4 and 5 min, respectively, the layer was stamped with a set of 12 electrodes. This process was repeated for seven elastomer layers and six electrode layers, producing 12 stacks of five active layers each (the outer two elastomer layers serve only as encapsulating layers, and do not actuate). Each of the 12 stacks was then manually punched out using a 17.5 mm hammer-driven hole punch, cutting through the connection tabs. The 12 stacks were combined into a taller stack by aligning them visually and laying them on top of each other, ensuring that no creases or bubbles were present. Colloidal graphite paint was applied to the side walls of the meta-stack where the connection tabs' cross sections were exposed. More graphite paint was used to electrically connect highly flexible 40 AWG wires to the tabs. These flexible wires were used to provide power and approximate free boundary conditions on the device and facilitated the manipulation of the stack. A droplet of P7670 precursor was then applied to the wires to mechanically affix them to the top of the stack.

*MDEA strain measurement:* A Phantom v2512 recorded the actuation of the MDEA at 4,000 fps with 1080p resolution. A custom Matlab image analysis program imported each frame and, using Canny edge detection, identified the edges of the image. Exterior edges were identified as those that were the maximum or minimum edge pixels in a given row or column. The average distance between these exterior edges was used to measure

strain in each direction relative to the distance in a resting frame. To account for transient, erroneous detections of edges, outliers were removed from distance measurements before the average was calculated.

*Elastomer layer thickness measurements:* Breakdown sample layer thicknesses were determined by cutting through the multi-layer structure and imaging the cross-section on an Olympus OLS4000 laser microscope. Measurements were made in the accompanying Olympus software by measuring the distance between manually placed reference lines on the electrodes that bound the central elastomer layer. We took one image from each of the three breakdown specimens.

*Statistical analysis:* Measurement values are reported as the mean value  $\pm$  one standard deviation. Sample sizes are denoted in the main text alongside reported values.

## REFERENCES

[1] *Markets and Markets, Electroactive Polymer Market by Type (Conductive Plastic, Inherently Conductive Polymer, Inherently Dissipative Polymer), Application (ESD Protection, EMI Shielding, Actuators, Capacitors, Batteries, Sensors), and Region - Global Fore.*

[2] Chortos, A., Hajiesmaili, E., Morales, J., Clarke, D.R., and Lewis, J.A. (2020) 3D Printing of Interdigitated Dielectric Elastomer Actuators. *Adv. Funct. Mater.*, 30 (1), 1907375.

[3] Kiil, H.-E., and Benslimane, M. (2009) Scalable industrial manufacturing of DEAP. 72870R.

[4] Kolloche, M., and Kofod, G. (2010) Electrical failure in blends of chemically identical, soft thermoplastic elastomers with different elastic stiffness. *Appl. Phys. Lett.*, 96 (7), 071904.

# 02 Thick polymer films with self-healing, UV-protection, and anti-fog properties

N. H. Kashem, X. Liu, Z. Ding, *et al.*

A high-performance and multifunctional layer-by-layer (LbL) film was fabricated by using a spin-spray-assisted (SSA-LbL) assembly method with poly(diallyldimethylammonium chloride) (PDDA) and poly(acrylic acid) (PAA). The SSA-LbL method was found to be more efficient and a time-saver in making a homogeneous thick film in tens of micrometers. When scratches occur, the film shows a quick and durable self-healing capability due to the dynamic movement of the flexible polyelectrolyte complex chains at the edges of the scratches. An effective UV-block performance was incorporated into the film by using graphene oxide (GO) and titanium dioxide (TiO<sub>2</sub>) nanoparticles. Due to the hydrophilic feature of PDDA/PAA molecules, the film also showed anti-fog properties in different environmental conditions.

## INTRODUCTION

Incorporating multiple functionalities in a film requires sophisticated surface design techniques. Usually, multifunctional thin film coatings are fabricated using techniques such as layer-by-layer (LbL) film deposition due to the advantages of facile fabrication technique, cost-effective process, and broad application areas.<sup>[1]</sup> The fabrication methods of LbL films include immersive, spin, and spray techniques, which are all based on the deposition of oppositely charged species on a specific substrate.

The immersive method has the problems of material wastage and time consumption. Additionally, it is not feasible for applications that need film coatings with micrometer thickness. The spin coating has been widely used to disperse the high-viscosity materials on the pla-

nar substrate and create highly organized multilayers.<sup>[2,3]</sup> The spray coating offers the advantage of easy up-scalability.<sup>[4]</sup> Herein, an SSA-LbL film assembly technique was developed to fabricate a thick polymer film considering time and material-saving and compared with other LbL assembly methods. Using the SSA-LbL technique, a novel multifunctional LbL film with self-healing, UV-protective, and anti-fog properties has been prepared using poly(diallyldimethylammonium chloride) (PDDA) as polycation and poly(acrylic acid) (PAA) as polyanion.<sup>[5,6]</sup>

One of the unique properties of LbL-assembled multilayer films is the ability to self-heal. Due to the dynamic chemical bonds, the PDDA/PAA film showed intrinsic self-healing behavior when it is in contact with water or exposed to high relative humidity.

Due to increasing environmental pollution and ozone layer depletion, serious health risks such as skin cancer are increasing due to UV radiation.<sup>[7,8]</sup> Hence, products with UV protection have been applied to industries, such as cloth, umbrellas, and sunhats. UV-protection coating is an approachable method to achieve UV shielding by adding specific functional additives. In addition, antifog surface coatings are an attractive and widely focused topic in material research as this phenomenon regularly occurs in our daily lives, causing inconveniences such as reduced visibility and security. In this study, as PDDA and PAA are both polyelectrolytes, the film is expected to absorb water and function as an antifog surface.

## EXPERIMENTAL

PDDA (Mw <10,000) and PAA (Mw = 10,000, 20 wt% aqueous solution) were obtained from Sigma. GO (C/O = 3.49, 5 mg/mL aqueous solution, 0.7–1.2 nm thickness) was obtained from the Goographene Company. TiO<sub>2</sub> nanoparticles (10–30 nm) were purchased from Skyspring Nanomaterials, Inc., and deionized (DI) water was used as the solvent.

The polycation solution was prepared by mixing PDDA (1 and 10 wt%) solution with GO dispersion solution (1 mg/mL) under continuous stirring. The pH was adjusted to 10.5 with 1 M HCl and 1 M NaOH after stirring for 1 h at room temperature. The polyanion solution was prepared by mixing the TiO<sub>2</sub> particle suspension with the PAA solution. First, TiO<sub>2</sub> nanoparticle suspensions (0.5, 2, 3, and 4 mg/mL) were prepared by ultrasonic homogenizer (VWR Analog Vortex Mixer, Marshall Scientific, United States). Then, the PAA solution (5 and 1 wt%) was added to the different concentrations of nanoparticle suspensions, respectively. The pH of the prepared solution was tuned to 3.0 with HCl (1 M) and NaOH (1 M).

A quartz slide was plasma treated for 10 min after cleaning with acetone. The first layer of LbL film was prepared by spraying the dispersion of PDDA-GO on the quartz slide for 5 s with a fixed height of 20 cm (Master Airbrush G22, United States), followed by putting the slide on the spin-coating machine (Laurell WS-650MZ- 23NPPB, United States) with the 3 steps program. First, 2,000 rpm for 40 s to ensure the polyelectrolyte solution is evenly distributed on the substrate; then, the substrate was rotated at different spin rates (2,000, 3,000, 4,000, and 5,000 rpm) for 1 min to split

out the excess polyelectrolyte solution. Finally, the surface of the sample was dried by rotating at a rate of 1,000 rpm for 30 s. The second layer was made by spraying the suspension of PAA-TiO<sub>2</sub> on the first layer for 5 s, similar to the abovementioned spin-coating program. The procedure was continued until the expected number of bilayers was achieved. In this process, the PDDA-GO/ PAA-TiO<sub>2</sub> film was referred to as (PDDA-GO/PAA-TiO<sub>2</sub>)\*n, where n represents the number of deposited bilayers.

Roughness of the films was measured through AFM (Veeco/Digital Instruments, United States) with a silicon nitride oxide-sharpened tip (NXHR, Nano-sensors, Germany). The position in the middle of each sample was imaged in tapping mode with a frequency range of 200–300 kHz on morphology.

A profilometer (DektaXT, Bruker Nano, United States) was used to measure the thickness of different films. Moreover, the film growth kinetics was investigated by varying the concentrations of PDDA and PAA.

The cross-section of the films and the surface structure in the self-restoration process were studied using scanning electron microscopy, SEM (Hitachi S-4300, Japan). The film was cut on the backside of the glass substrate and broken up by the hand. The samples were coated with gold and scanned under SEM at 350x, 1,500x, and 10,000x magnifications.

The self-healing property was evaluated using two protocols: (a) healing at a relative humidity (RH) of 80% and (b) healing in DI water. In test (a), the film on the glass substrate was cut with 40 μm of scratch on the surface, which was allowed to heal in a humidity-controlled glovebox (Electro-Tech Systems 5503-11 Mini Glove Chamber) at 25 °C (77 °F). The images of healing at the RH of 80% at various times were snapped by the transmitted microscope (EVOS imaging systems AMEFC4300). In test (b), a similar 40 μm of the scratched film was immersed in the DI water at 25 °C (77 °F) for 40 s to heal the scratch. The whole process of self-healing was recorded by the Olympus BV53 microscope system. The percentage of cut recovery and recovery speed can be measured by using the following expressions:

$$\text{Recovery \%} = \frac{d_0 - d_n}{d_0} \times 100$$

$$\text{Recovery speed} = \frac{\text{Recovery \%}}{t}$$

where  $d_0$  is the width of the original cut, and  $d_n$  is the width of the cut after a certain time.

The transparency of the film was evaluated using a photo test. Photographs were taken using a GoPro (7<sup>th</sup> generation) with an object 2 m (6.6 ft) behind the film samples with different concentrations of additions in polyelectrolyte solutions, PDDA + GO (1 mg/mL)/PAA + TiO<sub>2</sub> (1 mg/mL) and PDDA + GO (1 mg/mL)/PAA + TiO<sub>2</sub> (2 mg/mL) with 10 bilayers. In this process, the visibility of the object, situated behind the samples, can be used to evaluate the degree of transparency.

The optical properties of the films were investigated using a NanoDrop with a UV-vis spec-

trophotometer (Thermo Fisher Scientific) in the range of 200–500 nm. The percentage of transmittance of the film in the ranges of 290–320 nm (UV-B) and 320–400 nm (UV-A) was imaged using the instrument.

Characterization of the anti-fog property was evaluated using two protocols: a warm-fog and a cold-fog test. In the warm water test, the uncoated glass slides, and coated glass slides were put on an empty Petri dish situated on a piece of paper with the word "anti-fog." After adding warm water to the Petri dish, the visibility of the letter could be used to evaluate the degree of anti-fog. In the cold-fog test, coated and uncoated substrates were put in a refrigerator (<20 °C (68 °F)) for 5 min and

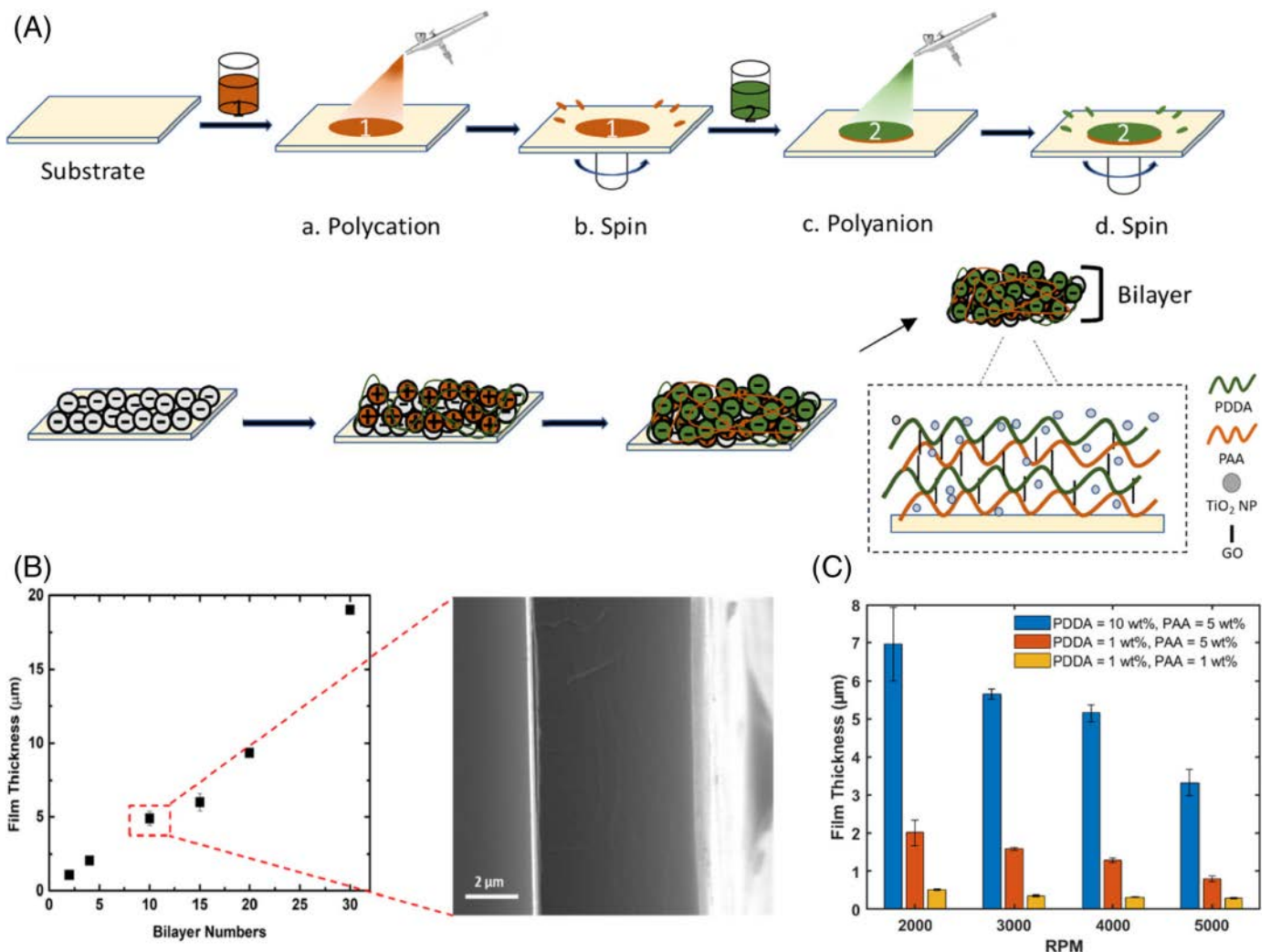


**Figure 1:** (A) Schematic illustration of spin-spray-assisted layer-by-layer assembly technique. (B) Thickness of the film as a function of bilayer numbers (left); SEM image of the cross-section of the film with 10 bilayers (right); (C) Thickness of the film as a function of spin rate (RPM) of the second step for different concentrations of the PDDA and PAA solutions.

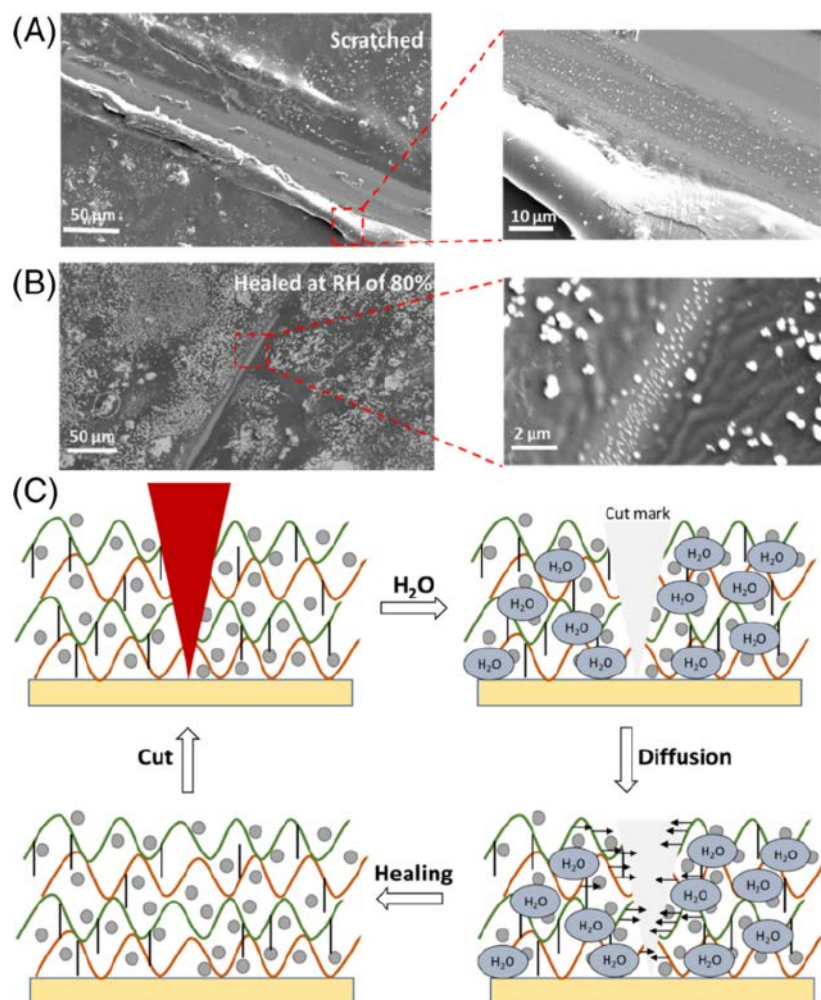


**Figure 2:** Self-healing process and mechanism of 10 bilayers of PDDA + GO/PAA + TiO<sub>2</sub> film. (A) A scratched film with 40 μm cut; (B) Healed film at the RH of 80% for 20 min; (C) Schematics of the cut-healing process. Green line, orange line, gray circle, black line, and red triangle represent the PAA, PDDA, TiO<sub>2</sub> nanoparticle, GO, and cut, respectively. The concentration of GO in the PDDA solution and TiO<sub>2</sub> in the PAA solution was both 1 mg/mL.

returned two substrates to the room temperature environment to do the visibility evaluation.

The water contact angle of coated and uncoated quartz slide was measured using an optical tensiometer (Attention Theta Lite, Biolin Scientific, Sweden). The water droplet was added to the surface of both samples using a syringe (diameter = 0.82 mm).

## RESULTS AND DISCUSSION

### Thickness growth of the LbL film

The scheme of the fabrication process of the films is shown in **Figure 1A**. The negative charges were obtained by applying oxygen plasma on the substrate, which attracts the positive charges on PDDA to launch the LbL process. When the surface of the film was cationic, the negatively charged PAA was attracted to the slide (green circles). The

complex layer that is made of PDDA with GO and PAA with TiO<sub>2</sub> is referred to as one bilayer of PDDA + GO/PAA + TiO<sub>2</sub> film.

The thickness of the film increased linearly below 10 bilayers following exponential growth above 10 bilayers. As displayed in the cross-section SEM images (**Figure. 1B**), the boundaries of each layer cannot be observed, hence, it can be inferred that a homogeneous cross-section structure was obtained. Such homogeneous morphology indicates that each layer of polyelectrolyte diffuses well into the interior of films during the spin-spray process. The thickness growth was further investigated by varying the spin RPMs of the second step under different concentrations of PDDA and PAA. The bilayer number was kept constant (10 bilayers). It was observed that the thickness decreases with the increase in spin rate. On the other hand, the thickness of the film decreased

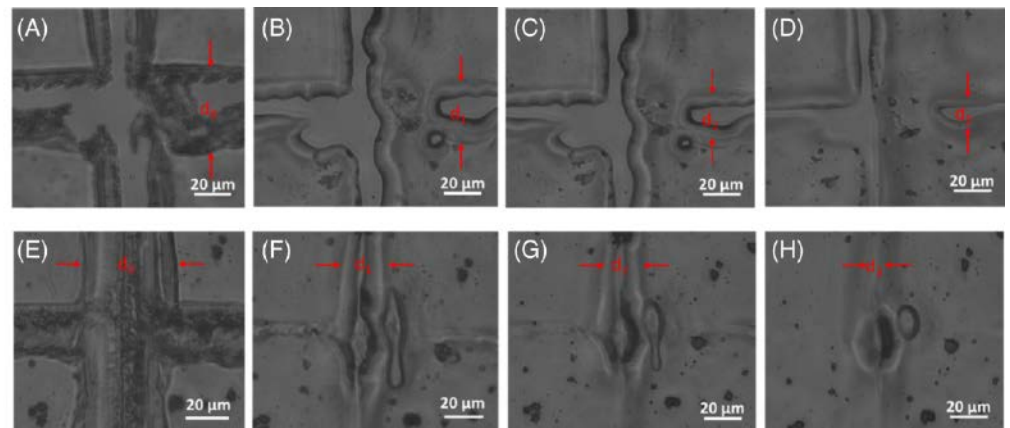
with the decrease in the concentration of the polyelectrolyte solutions (Figure 1C).

### SELF-HEALING PROPERTY

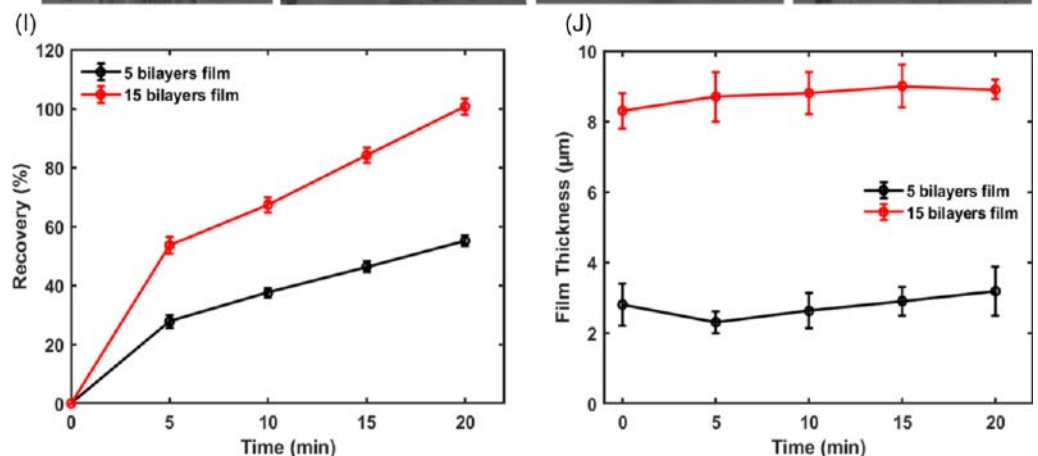
As shown in Figure 2A, a film of 10 bilayers was scratched with a 40  $\mu\text{m}$  cut, and the film segments of the cut were separated from the substrate. The film was put in the humidity chamber at RH of 80% for 20 min. To observe the surface structure of the PDDA + GO/PAA + TiO<sub>2</sub> film, gathered segments were tiled on the substrate. It was observed that most of the area of the scratch was healed (Figure 2B). When the scratched film was kept in the humidity chamber, the film absorbed moisture that was attracted by the carboxylic acid group and hydroxy group in the LbL film. With the joining of the water molecules in the film structure, the electrostatic force and hydrogen bonds were weakened, and the edges of the film became swollen and soft during this process. Meanwhile, the loose chains of PDDA and PAA diffused into the edges of the scratches

to close the gap and reform the polymer network. The film utilized the diffusion of polyelectrolytes and interactions between the chemical bonds, which include the reversibility of covalent and non-covalent bonds to rearrange the polymer chains and restore the destroyed interactions at damaged interfaces in the healing process. Moreover, we also investigated the healing behavior of the film in water. An LbL film with 40  $\mu\text{m}$  wide scratches was immersed in the DI water for only 40 s, and the cut was healed. Moreover, the film was cut several times in the same areas, and the cut film was able to recover every time after each cut.

For PDDA + GO/PAA + TiO<sub>2</sub> film, the healing process was triggered by using water or humid air to accelerate the mobility of polymer chains. We used two samples with different thicknesses, five bilayers of approximately 3  $\mu\text{m}$  and 15 bilayers of approximately 8  $\mu\text{m}$ , to explore the effect of thickness and deposition cycles on the self-healing behavior at the RH of 80%. As displayed in Figures 3A and 3E, a 40  $\mu\text{m}$  wide cut was made



**Figure 3:** The effect of film thickness on the recovery speed of PDDA + GO/PAA + TiO<sub>2</sub> film at the relative humidity of 80%. (A–D) and (E–H) are the microscope images of the self-healing process of 5-bilayer and 15-bilayer films at 0, 5, 10, and 15 min, respectively; D0, D1, D2, and D3 are the width of cuts on the films at 80% RH for corresponding time; (I, J) are the changing of recovery speed and thickness of 5-bilayer (black line) and 15-bilayer (red line) films as the function of time. The concentration of GO in the PDDA solution and TiO<sub>2</sub> in the PAA solution was both 1 mg/mL.



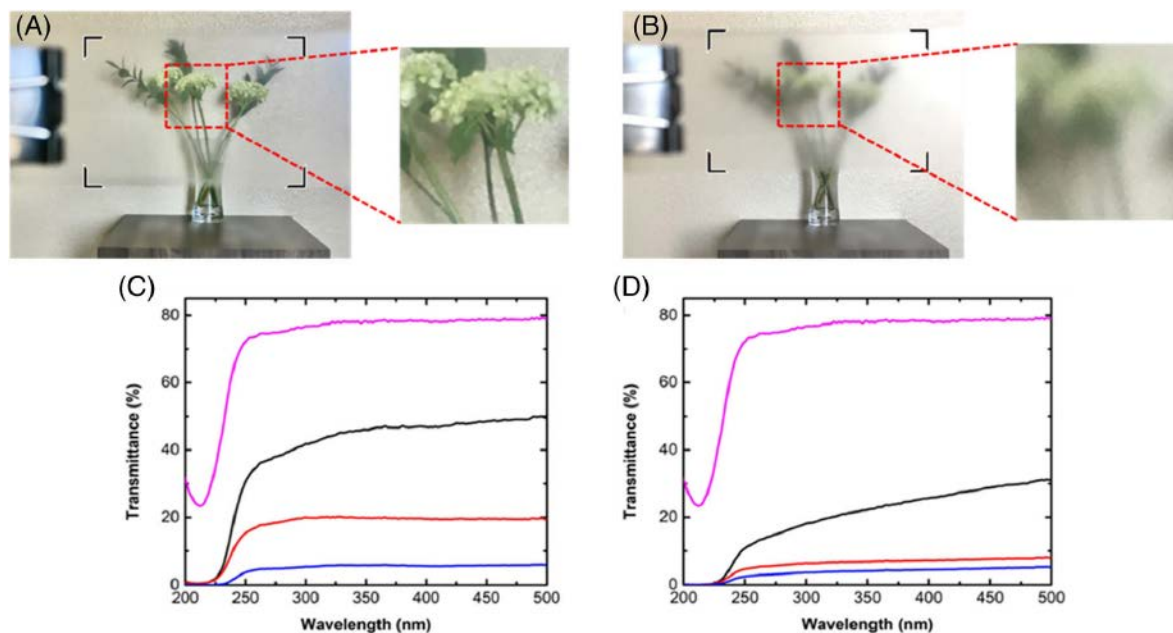


**Figure 4:** (A) Transparency of PDDA + GO (1 mg/mL)/PAA + TiO<sub>2</sub> (1 mg/mL) film; (B) Transparency of PDDA + GO (1 mg/mL)/PAA + TiO<sub>2</sub> (2 mg/mL) film; (C) UV-vis spectra of PDDA/PAA-TiO<sub>2</sub> film with different concentration of TiO<sub>2</sub> in PAA solution; (D) UV-vis spectra of PDDA + GO (1 mg/mL)/PAA-TiO<sub>2</sub> film with different concentration of TiO<sub>2</sub> in PAA solution. Pink line, black line, red line, and blue line represents the concentration of TiO<sub>2</sub> nanoparticles for 0, 1, 4, and 6 mg/mL, respectively.

on the 5 bilayers and 15 bilayers of PDDA + GO/PAA + TiO<sub>2</sub> film, respectively. After healing at 80% RH and room temperature for 5 min, the width of the cut on 5 and 15 bilayers film decreased to 30 and 20 μm, respectively as shown in **Figures 3B** and **3F**. After 15 min of healing, the cut on the 15-bilayer film almost disappeared at that condition.

According to the data shown in **Figure 3I**, the cuts on the 5- and 15-bilayer films were recovered for 25% and 55%, respectively, after placing the scratched films in the humidity chamber for 5 min. After healing for 20 min, the 15-bilayer film was fully recovered, and the 5-bilayer film still presented 45% of the width of the cut left. The recovery speed of two scratched films can be obtained by measuring the slope of the trendlines in **Figure 3I**. A 2-stage healing process including (1) water absorption and swelling and (2) polymer chain movement and rearrangement was found for both films. Moreover, the overall thickness across the different areas of the film did not change significantly during the healing time as shown in **Figure 3J**, which confirmed that the process of absorbing the water mol-

ecule primarily occurred at the edges of cuts and triggered the healing of surface damage, while the absorption of water and swelling in the non-damaged area could be neglected.

### Roughness

The roughness of the 5-bilayer film was measured as 42.3 nm; additionally, some aggregations and wrinkles were also observed on the surface. On the other hand, the roughness of the 15-bilayer film was around six times lower than the 5-bilayer film, although the form of wrinkles did not fully disappear when the number of depositions increased. The number of bilayers of LbL assembly films higher than 10 ensured the homogeneity of the film surface.

### Transparency and UV-resistance

Two samples were prepared with different TiO<sub>2</sub> concentrations as PDDA + GO (1 mg/mL)/PAA + TiO<sub>2</sub> (1 mg/mL) and PDDA + GO (1 mg/mL)/PAA + TiO<sub>2</sub> (2 mg/mL) with 10 bilayers. The PDDA + GO (1 mg/mL)/PAA + TiO<sub>2</sub> (1 mg/mL) film has fair transparent properties as the flowers could be seen from a distance of 2 m (6.6 ft). However, the segment of the flowers cannot be observed through the PDDA + GO

(1 mg/mL)/PAA +- TiO<sub>2</sub>-nanoparticle (2 mg/mL) film (**Figure 4**). According to the sharpness measurement of the two photographs, the PDDA + GO (1 mg/mL)/PAA + TiO<sub>2</sub>- (1 mg/mL) film (sharpness = 3.9914) is sharper than the PDDA + GO (1 mg/mL)/PAA + TiO<sub>2</sub> (2 mg/mL) film (sharpness = 1.4819). Therefore, the higher content of TiO<sub>2</sub> nanoparticles in the polyelectrolyte solution made the film less transparent and decreased its sharpness.

Next, the UV-resistant property of the LbL film was investigated by varying the concentration of TiO<sub>2</sub> in the film. First, the TiO<sub>2</sub> nanoparticles were blended in a PAA solution at pH 3.0 to make the TiO<sub>2</sub> suspension in an anionic solution. For the reference film made of PDDA/PAA, the percentage of transmittance of the UV light at 200 nm is 30%. After adding 1 mg/mL TiO<sub>2</sub> nanoparticles into PAA solutions, around 53% of the UVB (290–320 nm) and UVA (320–400 nm) can be blocked by the PDDA/PAA + TiO<sub>2</sub> LbL film. With the content of TiO<sub>2</sub> nanoparticles increased to 6 mg/mL, the UV light can be shielded more than 95% for UVA and UVB. Therefore, the UV-shielding effect showed great improvement with the increasing content of TiO<sub>2</sub> nanoparticles in the PAA solution. However, when the content of TiO<sub>2</sub> nanoparticles increased to 2 mg/mL, the transmittance of visible light decreased. To overcome this limitation, GO was considered to be added to the PDDA solution to achieve the transmission of visible light through the film with suitable UV resistance. According to the exploration of Xie et al.<sup>[9]</sup>, GO can block up to 97.5% of the UV light with 1.2 wt% for a single layer of the GO/PVA film and has a better transmittance of visible light than TiO<sub>2</sub> nanoparticles. Therefore, GO (1 mg/mL) was mixed with the PDDA solution at pH 10.5 to enhance the property of UV protection and transparency. As displayed in **Figure 4D**, more than 80% of UVB and more than 75% of UVA can be absorbed on PDDA + GO (1 mg/mL)/PAA + TiO<sub>2</sub> (1 mg/mL) film with 10 bilayers, which is significantly better than that of PDDA (No GO)/PAA + TiO<sub>2</sub> film of the same concentration (50% blocking of UVA and UVB). As a result, the LbL film with 1 mg/mL TiO<sub>2</sub> and 1 mg/mL GO concentration showed both suitable transparency and the UV-performance. The UV-blocking property was further improved with the increase in TiO<sub>2</sub> concentration as shown in **Figure 4D**. With 4 mg/mL TiO<sub>2</sub>, the film can block more than 95% of UVA and UVB, which is a significant improvement over the PDDA (no GO)/ PAA + TiO<sub>2</sub> (4 mg/mL) film. Hence, the film can be used for different purposes, for example, making

a higher UV-resistant surface without transparency or a moderate UV-resistant surface (more than 80% of UVB) with transparency.

#### Anti-fog property

After infusing the hot water under the samples, the condensing water droplets appeared on the unmodified glass slide. In contrast, the PDDA + GO/PAA + TiO<sub>2</sub> film can spread water to form a thin water layer and remain transparent behind the hot water. Second, a cold-fog examination was conducted to characterize the property of frost remaining and anti-fog in extremely cold conditions. An extremely thin ice membrane could be observed on the PDDA + GO/PAA + TiO<sub>2</sub> film. The modified glass substrate remained transparent due to the hydrophilic surface. However, the uncoated glass slide formed a fog on the surface due to the condensation of moisture in the air, and the unmodified glass slide became blurred. According to the contact angle measurements on the uncoated and coated substrates, the contact angle was lower on the coated surface than that on the uncoated surface. When the film was put in a high-humidity environment, the uniform water membrane could prevent the formation of fog to avoid light scattering.

## CONCLUSION

We obtained a multifunctional thick LbL film with self-healing, UV-blocking, and anti-fog properties using a spin-spray-assisted (SSA-LbL) assembly technique. This novel fabrication method was used by combining the spray and spin method to make a homogeneous LbL film with a high concentration of polyelectrolyte solutions that has the advantages of time- and material-saving compared with the traditional fabrication methods for LbL films. We provided evidence that the multifunctionality of the film can be achieved by incorporating the GO and TiO<sub>2</sub> nanoparticles with polycation and polyanion solutions, respectively. This multifunctional LbL film can be potentially used as a high-performance and long-lifespan coating in sports goggles, car windows, glass houses, etc., under various environmental conditions.

## REFERENCES

- [1] Esser-Kahn, A.P., Sottos, N.R., White, S.R., and Moore, J.S. (2010) Programmable Microcapsules from Self-Immolative Polymers. *J. Am. Chem. Soc.*, 132 (30), 10266–10268.
- [2] Merrill, M.H., and Sun, C.T. (2009) Fast, simple and efficient assembly of nanolayered materials and devices. *Nanotechnology*, 20 (7), 075606.
- [3] Tan, W.S., Cohen, R.E., Rubner, M.F., and Sukhishvili, S.A. (2010) Temperature-Induced, Reversible Swelling Transitions in Multilayers of a Cationic Triblock Copolymer and a Polyacid. *Macromolecules*, 43 (4), 1950–1957.
- [4] Wang, K., Hohn, N., Kreuzer, L.P., Widmann, T., Haese, M., Moulin, J.-F., and Müller-Buschbaum, P. (2019) Morphology Tuning of ZnO/P3HT/P3HT-*b*-PEO Hybrid Films Deposited via Spray or Spin Coating. *ACS Appl. Mater. Interfaces*, 11 (11), 10998–11005.
- [5] Syed, J.A., Tang, S., Lu, H., and Meng, X. (2015) Smart PDDA/PAA multilayer coatings with enhanced stimuli responsive self-healing and anti-corrosion ability. *Colloids Surfaces A Physicochem. Eng. Asp.*, 476, 48–56.
- [6] Yuan, T., Cui, X., Liu, X., Qu, X., and Sun, J. (2019) Highly Tough, Stretchable, Self-Healing, and Recyclable Hydrogels Reinforced by in Situ-Formed Polyelectrolyte Complex Nanoparticles. *Macromolecules*, 52 (8), 3141–3149.
- [7] Sharma, P., Montes de Oca, M.K., Alkeswani, A.R., McClees, S.F., Das, T., Elmets, C.A., and Afaq, F. (2018) Tea polyphenols for the prevention of UVB-induced skin cancer. *Photodermatol. Photoimmunol. Photomed.*, 34 (1), 50–59.
- [8] Wolf, S., Krensel, M., Mohr, N., Augustin, M., and Andrees, V. (2022) Effects of workplace skin cancer screenings on preventive and risk behaviour. *J. Public Health (Bangkok)*, 30 (9), 2243–2251.
- [9] Xie, S., Zhao, J., Zhang, B., Wang, Z., Ma, H., Yu, C., Yu, M., Li, L., and Li, J. (2015) Graphene Oxide Transparent Hybrid Film and Its Ultraviolet Shielding Property. *ACS Appl. Mater. Interfaces*, 7 (32), 17558–17564.

# 03 Enhancing the properties of electrodeposited copper foils by composite additives

S. P. Wang, K. X. Wei, W. Wei, *et al.*

It is urgent to develop copper foils with low surface roughness, high tensile strength, and suitable thermal conductivity in electronic equipment communication. Herein, the effect of three single additives (gelatin, polyacrylamide, and thiourea) and two composite additives (gelatin-polyacrylamide and thiourea-polyacrylamide (Tu-PAM)) on the surface roughness, tensile strength, and thermal conductivity of copper foil fabricated using direct current electrodeposition is investigated. We found that the ionic interaction and the deposited particle size play an important role in enhancing surface roughness and tensile strength.

## INTRODUCTION

Copper foils play a “neural network” role in electronic equipment communication and signal transmission.<sup>[1]</sup> However, the size of traditional metal conductors such as copper in the printed circuit board (PCB) has shrunk sharply, and signal transmission is concentrated on the surface of the conductors,<sup>[2]</sup> resulting in signal transmission failure, breakage, and continuous heating of the PCB.<sup>[3]</sup> It is urgent to develop copper foils with low surface roughness, high tensile strength, and good thermal conductivity simultaneously.<sup>[4]</sup>

Electrodeposition is one of the most important methods for preparing coating materials with excellent thermal, electrical, and mechanical properties.<sup>[5,6]</sup> Up to now, few reports are available on electrodeposited copper foils with low surface roughness, high tensile strength, and high thermal conductivity

simultaneously. This study aimed to report the effect of three single additives, namely gelatin (G), polyacrylamide (PAM), and thiourea (Tu), and two composite additives (G-PAM and Tu-PAM) on the microstructure and performance of copper foils produced by direct current electrodeposition and reveal a proper combination of the additives in the electrolyte.

Electrodeposition is one of the most important methods for preparing coating materials with excellent thermal, electrical, and mechanical properties.<sup>[5,6]</sup> Up to now, few reports are available on electrodeposited copper foils with low surface roughness, high tensile strength, and high thermal conductivity simultaneously. This research aims to study the effect of three single additives, namely gelatin (G), polyacrylamide (PAM), and thiourea (Tu), and two composite additives (G-PAM and Tu-PAM) on the microstructure and performance of copper foils produced by direct cur-

rent electrodeposition and reveal a proper combination of the additives in the electrolyte.

## EXPERIMENTAL SECTION

Copper plates (99.99%) and titanium plates (99.99%), with dimensions of 100×50×2 mm (3.9×2×0.08 in.) and 70×30×2 mm (2.8×1.2×0.08 in.), respectively, were used as anode and cathode. During electrodeposition, the current density was constant and equal to 90 mA cm<sup>-2</sup>, and the mechanical stirring rate was 120 rpm. The concentrations of additives G, PAM, and Tu were 20 mg L<sup>-1</sup>. The composite additives were G (10 mg L<sup>-1</sup>)-PAM (10 mg L<sup>-1</sup>) and Tu (10 mg L<sup>-1</sup>)-PAM (10 mg L<sup>-1</sup>). The copper foils were electrodeposited from the electrolyte CuSO<sub>4</sub>·5H<sub>2</sub>O (120 g L<sup>-1</sup>). The electrodeposition time was 60 min, and the pH value was controlled by H<sub>2</sub>SO<sub>4</sub>. The thickness of copper foils was about 70–80 μm.

The electrodeposition rate was calculated according to,<sup>[7]</sup>

$$v = \Delta m / s \cdot t \quad (1)$$

where  $\Delta m$ ,  $s$ , and  $t$  are the values of the quality change of the titanium plate before and after deposition (g), the area of the cathode plate (m<sup>2</sup>), and the electrodeposition time (h), respectively. X-ray diffractometer (D/max-2500 pc) was used to analyze the orientation and structure of copper foils, and the test ranges from 20° to 120°. The surface morphology of copper foils was characterized by a scanning electron microscope (Jeol JSM-IT100) with a working voltage of 20 kV. The surface roughness of copper foils was measured by a laser confocal microscope (Olympus LEXT OLS4100). The tensile properties of copper foil with a length of 20 mm and width of

2 mm were evaluated by a universal tensile testing machine (MTS Systems CO E44.104) with a heading velocity of 1 mm min<sup>-1</sup>.

The thermal conductivity of copper foils was calculated using Equation (2).

$$\lambda(T) = \alpha(T) \cdot C_p(T) \cdot \rho(T) \quad (2)$$

where  $\alpha(T)$ ,  $C_p(T)$ , and  $\rho(T)$  are thermal diffusivity, specific heat capacity temperature, and density, respectively. The laser thermal conductivity meter (Netzsch LFA-447) was used to test the thermal diffusivity of copper foils. A differential scanning calorimeter (Netzsch DSC-200-F3) was used to measure the specific heat capacity of copper foils in a temperature range from 25 to 65 °C (149 °F). Archimedes' method was used to calculate the density of copper foils.

## RESULTS AND DISCUSSION

Tu, after its addition, reacts with the free copper ions in the electrolyte to form Cu<sub>2</sub>S, which presents black or gray-black, resulting in a small number of bumps on the surface of copper foils and a slight darkening of the surface. After adding other additives, the surface of the prepared copper foils is smooth, without protrusions or holes.

Gelatin is a polarizer. It forms an adsorption film on the electrode surface. Cu<sup>2+</sup> must pass through this film to discharge on the electrode, i.e., to be deposited on the cathode plate. Therefore, the number of copper ions can be increased to improve the dispersion of the deposition solution, which is manifested as an increase in the deposition rate. On the other hand, Tu reacts with copper ions in the solution to form copper complex ions. This accel-

**Table 1:** Calculation results of the leveling capacity of six sedimentary liquids.

Sample	Substrate surface roughness [μm]	Copper foil surface roughness [μm]	Leveling ability [%]
No additive	2.613	2.337	10.6
G	2.481	1.502	39.5
PAM	2.267	1.676	26.1
Tu	2.837	3.017	-6.3
G+PAM	2.791	2.693	3.5
Tu+PAM	2.576	1.506	41.5

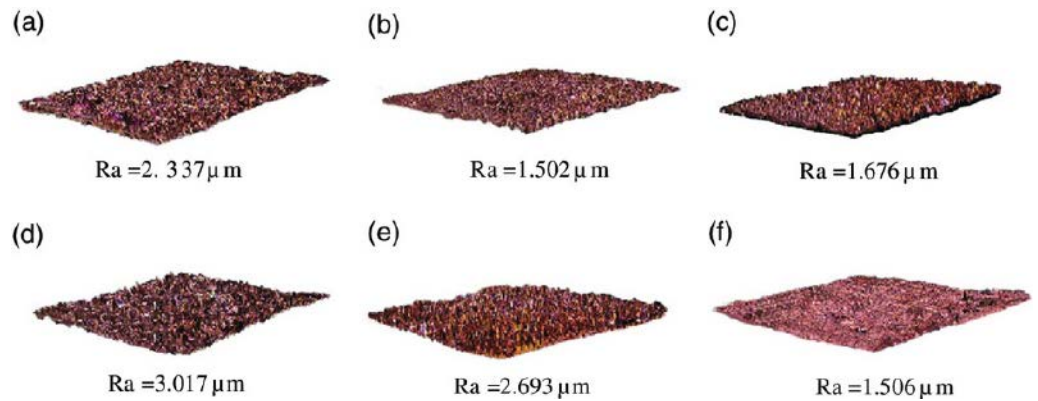


**Figure 1:** 3D profiles and surface roughness (Ra) of copper foils: a) without additives, and with additives of b) G, c) PAM, d) Tu, e) G-PAM, and f) Tu-PAM.

erates the formation of deposited particles, which is manifested as an increase in the deposition rate. When the additive is PAM, the carboxyl group in the PAM forms a polar bond or coordination bond with the copper ion, which increases the peak value of the copper deposition current, thereby increasing the deposition rate. When Tu and PAM coexist in the electrolyte, the electrodeposition temperature is 40 °C (104 °F), pH = 1.5, and the current density is 6 A dm<sup>-2</sup>. The two additives have a synergistic effect on the Cu<sup>2+</sup> reduction process, and jointly accelerate the deposition of copper. Hence, the copper foil has the highest deposition rate, reaching 514.4 g h<sup>-1</sup>m<sup>-2</sup>.

$$L = \frac{R_a - R_b}{R_b} \quad (3)$$

The deposited particles are significantly refined; in the case of high overpotential, the probability of crystal nucleus formation and the number of formed crystal nuclei are increased.

**Figure 1a–f** shows the 3D profile and surface roughness (Ra) of copper foils with different additives. Table 1 shows the calculation results of the leveling capacity of the six sedimentary liquids. The leveling ability (L) of the deposition solution can be calculated by

where Ra and Rb are the roughness of the substrate before electrodeposition and the roughness of the deposited product after electrodeposition, respectively. The surface roughness of the copper foils without additive, with G, and with Tu-PAM are 2.337 ± 0.208 μm, 1.502 ± 0.116 μm, and 1.506 ± 0.147 μm, and the electrolyte leveling ability increases to

39.5%, 26.1%, and 41.5%, respectively. Gelatin, a type of polarizer, can enhance polarization to improve the dispersion ability of the electrolyte, thereby forming fine Cu particles on the surface of the electrode, which is manifested as a reduction in surface roughness.<sup>[8]</sup> After adding Tu-PAM, -NH<sub>2</sub> will react with Cu<sup>2+</sup> in the solution to produce [Cu(NH<sub>4</sub>CS)]<sub>2</sub>SO<sub>4</sub> and Cu<sub>2</sub>S, which affects Cu deposition promotion when combined.<sup>[9]</sup> In addition, the wetting effect of the composite additives on the surface of the substrate causes the copper ion solution to diffuse in the recesses, which is manifested as an increase in crystalline active sites and an increase in the electrodeposition rate of copper.<sup>[10,11]</sup> Therefore, the recesses on the surface of the substrate are filled, the protrusions are weakened, and finally, the surface of the copper foil is much flatter.

The tensile test results are shown in **Table 2**. Compared with no additives, the tensile strength of copper foils is significantly improved after adding Tu-PAM. Simultaneously, the ductility is enhanced. The reduction in the size of the deposited particles results in the formation of more grain boundaries, which can function as a barrier to prevent the movement of dislocations and inhibit their displacement by generating a large amount of dislocation accumulation on grain boundaries. Therefore, the addition of Tu-PAM composite additive effectively reduces the size of the deposited particles, which has a significant contribution to the improvement of the tensile strength of the copper foils.<sup>[5]</sup>

**Table 2:** Tensile strength, uniform elongation, and thermal conductivity of copper foils.

Sample	Tensile strength [MPa]	Uniform elongation [%]	Thermal conductivity [ $\text{W m}^{-1} \text{K}^{-1}$ ]
No additive	164	2.6	391
G	200	3.6	212
PAM	231	2.6	354
Tu	198	1.8	240
G-PAM	273	2.3	146
Tu-PAM	256	2	356

The thermal diffusivity of copper foil prepared without additives is  $96.719 \text{ mm}^2 \text{ s}^{-1}$ , and after adding Tu-PAM, the thermal diffusivity of copper foil is  $100.655 \text{ mm}^2 \text{ s}^{-1}$ , which is an increase of about 4%. Without additives, the specific heat of the copper foil is  $0.458 \text{ J g}^{-1} \text{ K}^{-1}$ . After adding Tu-PAM, the specific heat is slightly reduced to  $0.398 \text{ J g}^{-1} \text{ K}^{-1}$ . The thermal conductivity of copper foil is affected by electron scattering.<sup>[12]</sup> Although the electron mobility of copper is relatively high, after adding Tu-PAM, due to the formation of complexes between  $\text{NH}_2$  and  $\text{Cu}^{2+}$ , a large number of dislocations will be generated in the copper foils, which will strengthen the scattering of electrons, thereby affecting the thermal conductivity of the copper foil to a certain extent.<sup>[13]</sup> Goli *et al.*<sup>[14]</sup> prepared the Gr-Cu-Gr heterogeneous film using the chemical vapor deposition method. It is found that the increase in grain size has a significant contribution to the improvement of the thermal conductivity of the heterogeneous film. Therefore, the decrease in thermal conductivity of copper foil prepared by adding Tu-PAM may be caused by the decrease in the size of the deposited particles. However,

the Tu-PAM composite additive compensates for the effect of electron scattering on thermal conductivity to a certain extent, because it effectively reduces the size of the deposited particles of copper and increases their density.

## CONCLUSIONS

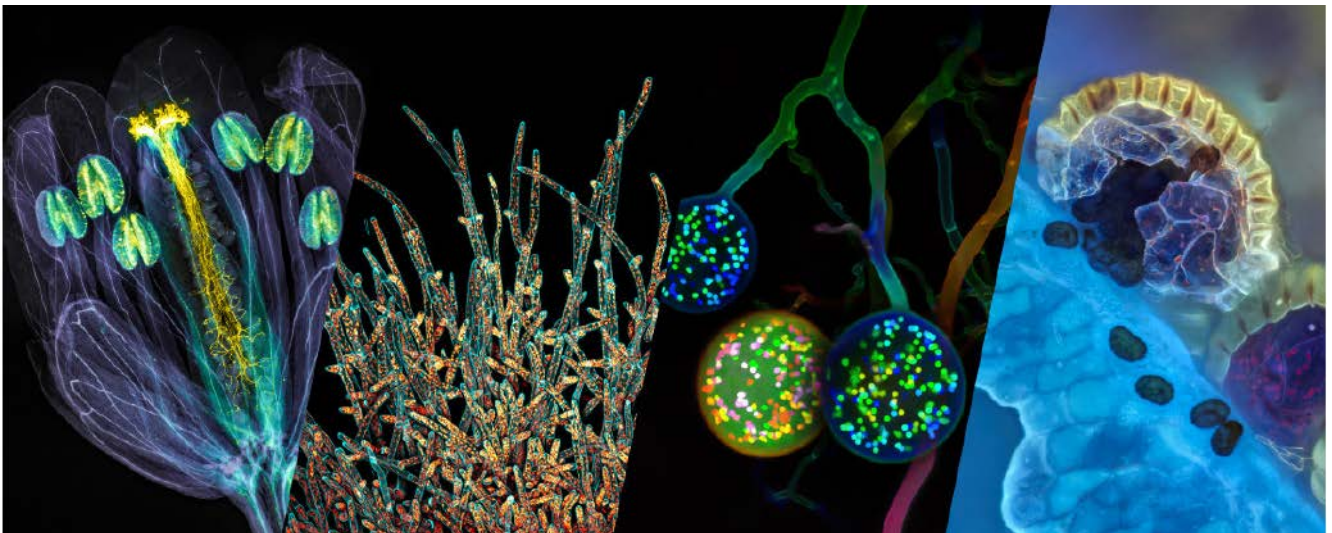
The results show that when Tu+PAM are added as composite additives to the electrolyte, compared with adding Tu and PAM separately, the deposited particles are finer, and the copper foil is flatter. We showed that two additives have a synergistic effect on the reduction process of copper ions. Adding Tu-PAM composite additive can effectively increase the deposition current density, thereby accelerating the formation of crystal nuclei, and reducing the size of the deposited particles of copper foils. The reason for variations in surface roughness and tensile strength is the ionic interaction and the size of the deposited particles.

## REFERENCES

- [1] Abbasi, M., Brown, D.A., Bernhard, T., Klaeden, K., Schulze, J.F., Zarwell, S., and Brüning, R. (2020) Microstructure of combined electroless and galvanic deposits on roll annealed copper foils and copper single crystals. *Thin Solid Films*, 714, 138366.
- [2] Kurzepa, L., Lekawa-Raus, A., Patmore, J., and Koziol, K. (2014) Replacing Copper Wires with Carbon Nanotube Wires in Electrical Transformers. *Adv. Funct. Mater.*, 24 (5), 619–624.
- [3] Zhang, Z., Wu, Y., Zhang, Y., Hang, T., Hu, A., Ling, H., and Li, M. (2019) Competitive Effect of Leveler's Electrochemical Behavior and Impurity on Electrical Resistance of Electroplated Copper. *J. Electrochem. Soc.*, 166 (13), D577–D582.
- [4] Wang, Z., Cai, X., Yang, C., and Zhou, L. (2018) Improving strength and high electrical conductivity of multi-walled carbon nanotubes/copper composites fabricated by electrodeposition and powder metallurgy. *J. Alloys Compd.*, 735, 905–913.
- [5] Yasin, G., Khan, M.A., Arif, M., Shakeel, M., Hassan, T.M., Khan, W.Q., Korai, R.M., Abbas, Z., and Zuo, Y. (2018) Synthesis of spheres-like Ni/graphene nanocomposite as an efficient anti-corrosive coating; effect of graphene content on its morphology and mechanical properties. *J. Alloys Compd.*, 755, 79–88.
- [6] Tabish, M., Malik, M.U., Khan, M.A., Yasin, G., Asif, H.M., Anjum, M.J., Khan, W.Q., Ibraheem, S., Nguyen, T.A., Slimani, Y., and Nazir, M.T. (2021) Construction of NiCo/graphene nanocomposite coating with bulges-like morphology for enhanced mechanical properties and corrosion resistance performance. *J. Alloys Compd.*, 867, 159138.
- [7] Yu, W., Lin, C., Li, Q., Zhang, J., Yang, P., and An, M. (2021) A novel strategy to electrodeposit high-quality copper foils using composite additive and pulse superimposed on direct current. *J. Appl. Electrochem.*, 51 (3), 489–501.
- [8] Chang, T., Jin, Y., Wen, L., Zhang, C., Leygraf, C., Wallinder, I.O., and Zhang, J. (2016) Synergistic effects of gelatin and convection on copper foil electrodeposition. *Electrochim. Acta*, 211, 245–254.
- [9] Allahyarzadeh, M.H., Aliofkhaezai, M., Rezvani, A.R., Torabinejad, V., and Sabour Rouhaghdam, A.R. (2016) Ni-W electrodeposited coatings: Characterization, properties and applications. *Surf. Coatings Technol.*, 307, 978–1010.
- [10] Kijlstra, J., Reihs, K., and Klamt, A. (2002) Roughness and topology of ultra-hydrophobic surfaces. *Colloids Surfaces A Physicochem. Eng. Asp.*, 206 (1–3), 521–529.
- [11] Bico, J., Thiele, U., and Quéré, D. (2002) Wetting of textured surfaces. *Colloids Surfaces A Physicochem. Eng. Asp.*, 206 (1–3), 41–46.
- [12] Jagannadham, K. (2012) Electrical conductivity of copper-graphene composite films synthesized by electrochemical deposition with exfoliated graphene platelets. *J. Vac. Sci. Technol. B, Nanotechnol. Microelectron. Mater. Process. Meas. Phenom.*, 30 (3), 03D109.
- [13] Jagannadham, K. (2012) Thermal Conductivity of Copper-Graphene Composite Films Synthesized by Electrochemical Deposition with Exfoliated Graphene Platelets. *Metall. Mater. Trans. B*, 43 (2), 316–324.
- [14] Goli, P., Ning, H., Li, X., Lu, C.Y., Novoselov, K.S., and Balandin, A.A. (2014) Thermal Properties of Graphene-Copper-Graphene Heterogeneous Films. *Nano Lett.*, 14 (3), 1497–1503.

# 04 The art of science: Evident image of the year award 2022

Evident has launched its 4<sup>th</sup> Global Image of the Year Scientific Light Microscopy Award



## Global Winner Image of the Year 2020

Werner Zuschratter (Germany) took the winning image. It is a three-channel, large-scale confocal image of a fixed and cleared rat embryo. Two channels show different autofluorescence sources of the tissue, while the third channel shows the skeleton stained by alizarin red.

Since its inception in 2017, the Image of the Year Award has become a highly esteemed event within the life science microscopy community. Each year, the competition continues to grow with hundreds of entries from across the globe, celebrating the beauty and creativity of the life science microscopy community. The award showcases the amazing work of microscopists and promotes a global appreciation for scientific images.

This year, the competition has broadened its scope to include images from materials science in addition to life science. Through this, the award seeks to demonstrate the beauty and versatility of the art of science. Submissions can be made by uploading up to three images, along with a description of the equipment used, at [Olympus-LifeScience.com/IOTY](https://Olympus-LifeScience.com/IOTY) until February 28, 2023.

Prizes include an Olympus SZX7 stereo microscope with a DP23 digital camera, X Line™ objectives for the global winner, an Olympus CX23 upright microscope, and an SZ61 stereo microscope for the winner of the new dedicated category for materials science and engineering images.

An expert jury of science and imaging professionals from around the world will assess all entries based on their artistic and visual aspects, scientific impact, and microscope proficiency. Winners will be chosen by a jury of leading experts in the field and announced in the summer of 2023.

If you are a budding scientist and have an eye for remarkable images, this is your opportunity to shine!